NANOMETER SCALE ATOMIC STRUCTURE OF ZIRCONIUM BASED BULK METALLIC GLASS

By

Jinwoo Hwang

A dissertation submitted in partial fulfillment of

the requirements for the degree of

Doctor of Philosophy

(Materials Science and Engineering)

at the

UNIVERSITY OF WISCONSIN – MADISON

2011

Table of Contents

Abstract

We have studied the nanometer scale structure of bulk metallic glass (BMG) using fluctuation electron microscopy (FEM). The nanometer scale medium range order (MRO) in BMG is of significant interest because of its possible relationship to the properties, but the experimental study of the MRO is difficult because conventional diffraction techniques are not sensitive to the MRO scale. FEM is a quantitative transmission electron microscopy technique which measures the nanoscale structural fluctuation associated with MRO in amorphous materials, and provides information about the size, distribution, and internal structure of MRO. In this work, we developed an improved method for FEM using energy-filtered STEM nanodiffraction with highly coherent probes with size up to 11nm in a state-of-the-art C_s-corrected STEM. We also developed an effective way to eliminate the effect of sample thickness variation to the FEM data by using Z-contrast images as references. To study the detailed structure of MRO, we developed a hybrid reverse Monte Carlo (H-RMC) simulation which combines an empirical atomic potential and the FEM data. H-RMC generated model structures that match the experimental data at short and medium range. In addition, the subtle rotational symmetries in the FEM nanodiffraction patterns were analyzed by angular correlation function to reveal more details of the internal structure of MRO. Our experiments and simulations show that Zr-based BMG contains pseudo-planar, crystal-like MRO as well as icosahedral clusters in its nanoscale structure. We found that some icosahedral clusters may be connected, and that structural relaxation by annealing increases the population of icosahedral clusters.

Chapter 1. Introduction

1. 1. Bulk metallic glass

Bulk metallic glasses (BMGs) are multi-component amorphous alloys which form by glass transition when quenched from metal liquids [1-3]. Since their first discovery, BMGs have drawn significant attraction because of their superior properties, such as high strength [4] and elasticity [5, 6], good corrosion resistance [7, 8] and biocompatibility [1], many of which exceed their crystalline counterparts [3]. In the past, the discovery of BMGs with higher glass forming ability (GFA), such as Zr and Pd based glasses, allowed the BMG fabrication in larger sizes up to ~10cm [2, 3], and BMGs based on inexpensive metals, such Fe, were also developed [9, 10]. There have also been advances in processing of BMGs, including the development of composites [4, 11, 12], foams [13-15], and net-shape forming techniques [16, 17]. Some BMG systems have already been commercialized [2, 3], and there are more possibilities for future applications in many frontier engineering fields, such as MEMS and nano-fabrication [18, 19].

The formation mechanism of BMGs can be best understood by the role of different atomic components in the system. According to empirical guidelines, there must be negative heat of mixing among the atomic components of a BMG, but preventing crystallization is also key [1, 2]. The most important factor to 'frustrate' the crystalline structure is the atomic size difference in a BMG system [2]. When the atomic size difference is large, the compositional windows for possible crystalline phases become smaller, so quenching which significantly drops the atomic mobility effectively prevents the nucleation and growth of a crystal. Another factor is the chemistry between the atomic species. The atomic bonding in a BMG must be mostly

metallic, but some chemical bonding characteristics apparently affect the GFA. For example, Cu and Ni are similar in atomic sizes, but the Zr-Cu-Al BMGs have a higher GFA than the Zr-Ni-Al BMGs [20, 21]. A recent Molecular Dynamics (MD) simulation suggested that the high GFA of Zr-Cu-Al BMGs is in part due to the "shortened" bond length between Cu and Al [22].

Understanding the details of the atomic structure of BMG is important, but only limited information from experiments is available so far. The structure factor, $S(k)$ where k is the scattering vector magnitude, can be measured by conventional diffraction experiments using x-rays, neutrons or electrons [23]. However, unlike in crystalline materials, the $S(k)$ from a BMG does not uniquely determine the structure because of the absence of long range order (LRO). Instead, the pair distribution function, $g_2(r)$, which is obtained from $S(k)$, shows the structure averaged over a coordination shell in a distant r, and it is frequently used for structural studies of amorphous systems [23]. However, the information from g_2 is limited to short range order (SRO), typically up to ~3rd coordination shell due to the inherent sampling problem [24]. The g_2 from a multi-component BMG is even more limited, because the g_2 is most useful when all partial g_2's are resolved [25], which is experimentally very difficult for multi-component systems. Extended x-ray absorption fine structure (EXAF) [26] or resonant x-ray scattering [25] can measure chemistry up to ~3 coordination shells, but still only provide a subset of the structure in SRO scale.

Computational simulations, on the other hand, have provided some useful insights about the structure of BMGs [22, 27-32]. Theoretical understanding of BMG structure evolved from a dense random packing of hard-sphere balls [27] to a jammed close-packed structure [28], and to a short range order (SRO) comprised of quasi-icosahedral atomic packing [22, 29-32]. Many molecular dynamics (MD) simulations have shown that the SRO in BMG is dominated by the

icosahedral clusters, each of which is locally energetically stable and close-packed [22, 29-32]. Sheng et al [31]. studied the structure of SRO clusters in their *ab initio* MD models by Voronoi tessellation [33], and found that both full icosahedra and quasi-icosahedral clusters are abundant in metallic glass systems [31]. They also suggested that the icosahedral clusters can connect to each other by corner, edge or face-sharing, and form a chain or a supercluster [22, 31]. The possible topology of the connections of the icosahedral-like clusters has also been studied by Miracle [30]. These computational studies imply that, in a metastable glass system where global energy minimization by forming LRO cannot be achieved, energy minimization likely occurs in a SRO scale by forming quasi-icosahedral clusters. The clusters cannot be periodically arranged because they are based on 5 fold rotational symmetry, but some connections between the clusters may be possible [34].

While we fundamentally agree that the high population of icosahedral clusters in BMGs is likely, we must question if the MD simulations generate a realistic BMG structure, especially at the nanometer scale. As Cheng et al. pointed out [22], a typical quench rate of MD simulations (~10^{13}K/s) may be too fast to generate a realistic nanoscale structure in the model. Compared to the simulations, a typical quench rate of BMGs in a lab environment is much slower (~10^{0} to 10^{5}K/s) [2], so more atomic motion is possible during the quenching, which may lead to an energy minimization in a longer length scale. This opens a possibility of medium range order (MRO), an order in between SRO and non-existing LRO, in real BMGs. MRO in BMG has been observed in some MD studies [30, 31, 35, 36], but the detailed structure of MRO remains unclear. Sheng et al. showed that the icosahedral clusters can gather and make MRO, the size of which can reach to about a nanometer [31]. However, more recent MD simulations

suggested that glasses may contain a nanoscale crystalline-like order which is incompatible to the icosahedral order [35, 36].

The nanometer scale MRO in BMG may be related to some of the BMGs' important behaviors, such as structural relaxation [37-39] and plastic deformation [40-42]. Like other glasses, BMGs undergo structural relaxation when annealed at a temperature below the glass transition temperature (T_g) [37]. The structural relaxation can be detected by differential scanning calorimetry (DSC) [38], but what structural change actually occurs in the atomic level is difficult to measure. The change in g_2 by structural relaxation is usually very small [39], which means little change in SRO, so we assume that the structural relaxation may involve a larger volume of material, possibly at the MRO scale. The current interpretation of this exothermic heat is the free volume annihilation [38], but the annihilation may be a result of a larger scale structural change, not a major mechanism of the relaxation.

Theories suggest that the deformation of a BMG starts from the shear transformation zones (STZs) which consist of a group of a few hundred atoms [41, 42]. When stress is applied, the STZs activate by undergoing shear deformation inside themselves for a limited distance (~ a few Å) [41, 42]. One STZ activation prompts other STZ activations nearby, and this forms a thin band-like deformed region called shear band [40-42]. At a low temperature compared to T_g, the shear bands localize in a small volume of the material, causing inhomogeneous deformation, but at high temperature shear bands spreads throughout the material leading to homogeneous deformation [40]. A shear band is about 50~100nm thick and easily observable in TEM [43], but the atomic structure inside the shear band is still not known, although there have been some indications that the atom density inside the shear band may be lower than a undeformed region

[43-45]. The diameter of STZs could be one to a few nanometers [41, 42], so it may have a relationship with the MRO in BMG.

We chose 3 different BMGs for this study: cast $Zr_{54}Cu_{38}Al_8$ [21], melt-spun $Zr_{50}Cu_{45}Al_5$ [46], and melt-spun $Cu_{64.5}Zr_{35.5}$ [32], which allowed us to investigate the effect of the compositional difference and quench rate on the MRO structure. We also studied how the thermal history of a BMG changes the MRO structure by a series of annealing experiments with the $Zr_{50}Cu_{45}Al_5$ and $Zr_{54}Cu_{38}Al_8$ BMGs.

1. 2. Fluctuation electron microscopy

Our experimental tool for measuring MRO in BMGs is fluctuation electron microscopy (FEM). FEM is a transmission electron microscopy (TEM) technique which measures structural fluctuations at the nanometer scale [47]. MRO, if it exists in an amorphous material, diffracts the electron beam following Bragg's law. Unlike the diffraction from crystals, however, the MRO diffraction is weak, because MRO is only one to a few nanometers in size, and not as strictly ordered as nanocrystals. Because of the low intensity and averaging over a very large number of nanometer-sized objects, the MRO signal does not stand out from the diffuse amorphous signal in a conventional, large-area diffraction. FEM captures the diffraction from MRO by measuring the normalized variance, *V*, among many diffracted intensity measurements made with nanometer spatial resolution, *I* [47].

$$V(k,R) = \frac{\left\langle I(k,R,\mathbf{r})^2 \right\rangle_{\mathbf{r}}}{\left\langle I(k,R,\mathbf{r}) \right\rangle_{\mathbf{r}}^2} - 1, \qquad \text{(Eq. 1)}$$

where k is the scattering vector magnitude, R is the FEM resolution, and $\langle \ \rangle_{\mathbf{r}}$ indicates averaging over position of the sample, **r**. Considering its nanometer scale size, MRO must have strong 3 or 4 body correlations, g_3 or g_4, on which V depends more than on g_2 [48]. V measures the structural fluctuation caused by the MRO, so if the degree of MRO is high, V will be high, but if the structure is homogeneous, V will be low [47]. Like in a conventional diffraction, the k position of the peaks in $V(k)$ is the inverse of an interatomic spacing of the order, d, so it contains the internal structural information of MRO. R sets the length scale of the fluctuation measured in FEM experiment, and by the Rayleigh criterion, $R = 0.61/Q$, where Q is the objective aperture (OA) radius in reciprocal space units. $V(k)$ as a function of R is variable resolution FEM (VRFEM), and it provides information about size and distributions of MRO [48, 49].

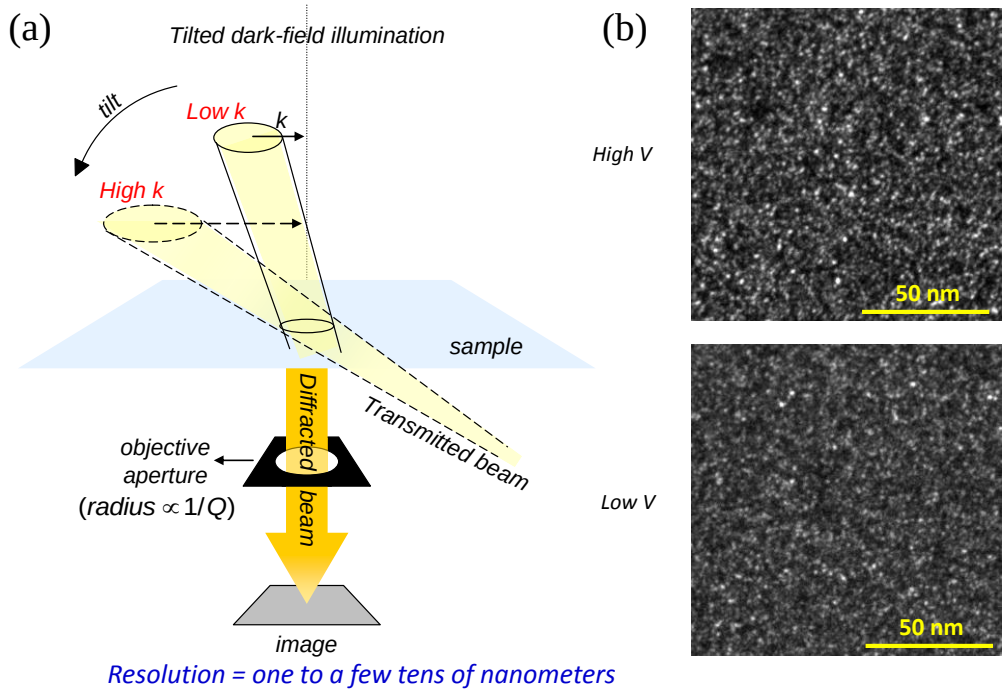

Figure 1. (a) Typical experimental configuration of FEM in CTEM, using tilted DF illumination. (b) Example FEM DF images from $Zr_{54}Cu_{38}Al_8$ BMG showing high V (above), and low V (below).

FEM can be performed either in conventional TEM (CTEM) or scanning TEM (STEM). CTEM FEM measures the MRO diffraction in real-space dark field (DF) images [47]. The physical size of the OA typically needs to be ~10μm or smaller to have an R of one to a few nanometers, and to capture diffraction in all angular 2π angles in one k, hollow-cone DF illumination mode is often used [47]. A series of DF images is acquired as a function of k by tilting the beam (Figure 1(a)), and V is calculated among the I's of each pixel for each k using Eq. 1. $V(k)$ from several DF series are typically averaged to increase statistical reliability. Figure 1(b) shows the examples of FEM DF images with high V (above) and low V (below).

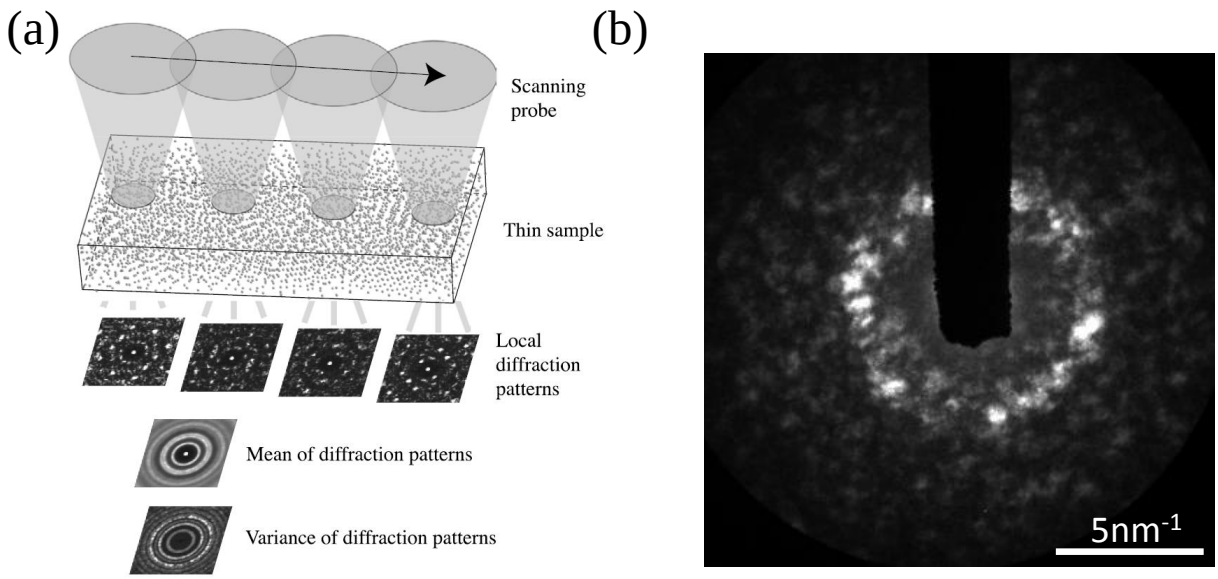

Figure 2. (a) Typical experimental configuration of FEM in STEM [47]. (b) Example nanodiffraction patterns acquired with 2nm probe from $Cu_{64.5}Zr_{35.5}$ BMG [50].

STEM FEM measures $V(k)$ based on the nanodiffraction using minimally convergent STEM probes, as shown in Figure 2. STEM FEM is optically conjugate to CTEM FEM, so it measures the same $V(k)$ but has many practical advantages over CTEM FEM [47, 49, 50]. First, the STEM probes have high spatial coherence, which increases the I peak from MRO and therefore maximizes V. Second, STEM FEM has very high k sampling because the $I(k)$ is obtained by the angular averaging of nanodiffraction patterns, as opposed to the CTEM FEM where the k sampling is limited by the beam tilt steps. Such higher k space sampling is important when studying a detailed and subtle structure of MRO. Third, VRFEM is much easier in STEM FEM because R can be changed electronically by changing lens excitations. In CTEM FEM, changing R requires using multiple OAs with physical sizes of 10μm or smaller, which is difficult in a typical CTEM. Finally, STEM FEM is often performed in newer machines with better stability, which coincides with the current trend of STEMs replacing CTEMs. Microscopes with better stability reduce problems such as sample drift or contamination. A disadvantage of STEM FEM is that it probes nanoscale volumes of samples one at a time, so even with hundreds of diffraction patterns, the sample volume examined is much smaller than that of CTEM FEM, which illuminates larger areas at once. This may in principle increase the uncertainty of measurement [47].

$V(k)$ provides intuitive understanding about the length scale of structural fluctuations in an amorphous material, but it is often necessary to extract more detailed MRO information, such as size, distribution, and internal structure from $V(k)$ to fully understand the material. However, directly connecting the $V(k)$ and the detailed MRO information is not always straightforward. Unlike g_2 which is obtained from $I(k)$ [23], the direct inversion from $V(k)$ to g_3 and g_4 is not a solved problem [48]. We have used the pair persistent model [48], and the amorphous /

nanocrystal composite model [51] to extract MRO information from the FEM data. One other method of extracting the MRO information is reverse Monte Carlo (RMC) simulation, which is discussed in detail in Chapter 4.

The pair persistent model provides size information of the MRO in the glass in the form of a correlation length Λ. It assumes that g_4 has a Gaussian decay envelope, $\exp(-|r|^2/2\Lambda^2)$ [48]. At low resolution, the model predicts $1/V$ vs. $1/Q^2$ is linear, so [48]

$$\frac{1}{V(k,Q)} = c + \frac{m}{Q^2}, \qquad \text{(Eq. 2)}$$

where m is the slope and c is the intercept of the linear fit. The correlation function decay length Λ is then

$$\Lambda = \frac{1}{2\pi}\sqrt{\frac{c}{m}}. \qquad \text{(Eq. 3)}$$

Λ is related to the radius of MRO [48]. The pair persistent model was tested using simulations of $V(k)$ from paracrystalline and continuous random network models of amorphous Si [48], where the Λ matched the relative extent of order that was originally introduced into the models. VRFEM experiments on amorphous Si were performed using STEM FEM [49, 52], and Bogle et al. found that the Λ's from the sputtered and the PECVD amorphous Si were nearly the same [52]. Q=0.61/R, so VRFEM data with at least 3 different R is needed to apply this model, and a large Q range is preferred to ensure reliable fitting in the Eq. 2. However, the model uses a same Q dependence for all k, so it assumes only one type of MRO, which may underestimate the different types of MRO in multi-component materials.

The amorphous / nanocrystal composite model provides information about the size and distribution of MRO [51]. The model makes the idealizing assumption that the structure can be modeled as a nanocrystal / amorphous matrix composite with uniform nanocrystal diameter d which is assumed to be smaller than R. This model predicts that [51],

$$V \approx \left\{ \frac{\frac{\pi}{6} C_{hkl} \Phi d^2 \left(d^3 \rho \pi / 6 \right)^2}{t \left[C_{hkl} \Phi \left(d^2 \rho \pi / 6 \right) + 1 \right]^2} \right\} \frac{1}{R^2}, \qquad \text{(Eq. 4)}$$

where ρ is the atom number density, Φ is nanocrystal volume fraction, and ($C_{hkl}d$) is proportional to the fraction of a randomly oriented population of nanocrystals that are near a Bragg reflection. C_{hkl} depends on experimental parameters like the spatial resolution R and on the crystal structure of the nanocrystals. Using this model, the contribution of each parameter, such as d and Φ, to V can be studied directly. When Φ is known, d can be calculated by [51],

$$d = \left(\sqrt{\frac{3}{2\pi} C_{hkl} \Phi t \Omega} + \left(1 + \sqrt{1 + \frac{4}{C_{hkl} \Phi t \Omega \rho} \sqrt{\frac{6 t \Omega}{\pi C_{hkl} \Phi}}} \right) \right)^{0.5}, \qquad \text{(Eq. 5)}$$

where Ω is the slope of the linear $V \sim 1/R^2$ relationship in Eq. 4. In the limit of large R, so that $R >$ d and $R >> \Lambda$, the two models predict the same behavior for V. However the relationship between the parameters of the two models is not simple. Λ is different from d because it depends on both d and Φ [53], and determining d and Φ from Eq. 4 requires C_{hkl} which needs substantial *a priori* knowledge of the structure [51]. As in the pair persistent model, large R range is important to have reliable fitting, but since R must be larger than d, it is more important to form larger probes with different sizes for the amorphous / nanocrystal composite model.

FEM has been used for studying the nanometer scale structures of various amorphous and glassy systems. FEM experiments and simulations showed that amorphous semiconductor thin

films, such as amorphous Si, Ge, and C, contain paracrystalline phases which are small and heavily strained, but have the same bonding patterns as the corresponding crystalline phases [54-57]. FEM have also detected the subcritical crystalline nuclei which drive crystallization upon heating in chalcogenide glasses, such as $Ge_2Sb_2Te_5$ [58]. Similar proto-crystalline nuclei MRO drives the primary crystallization reaction in Al-based marginal metallic glasses [59]. FEM on 5-component Zr-based BMGs showed measurable MRO [60]. The variances of several other types of fluctuations, or subject to different types of averaging, have also been reported [61, 62].

Chapter 2 describes the experimental methods for both CTEM FEM and STEM FEM. FEM experimental results from Zr-based BMGs is discussed in Chapter 3. We used RMC and hybrid RMC (H-RMC) simulations to study detailed atomic structure of MRO in BMG, which is discussed in detail in Chapter 4. Finally, we performed angular correlation analysis on the FEM nanodiffraction data to measure the subtle rotational symmetry to uncover more details about the internal structure of MRO. The angular correlation analysis is discussed in Chapter 5.

Chapter 2. Common Experimental Procedures

2. 1. BMG sample preparation

$Zr_{54}Cu_{38}Al_8$ [21] ingots (3mm in diameter, 40mm in length) were suction-cast and provided by our collaborators, Drs. Cao and Chang. $Cu_{64.5}$ $Zr_{35.5}$ [32] and $Zr_{50}Cu_{45}Al_5$ BMG ribbons [46] (~400μm thick) were formed by melt-spinning and provided by Drs. Kalay and Kramer. The quench rate was ~100K/sec for the suction casting, and ~10^5K/sec for the melt spinning with 25m/sec wheel speed.

For TEM sample preparation, the ingots were first cut with a Struers Accutom-5 diamond saw to ~500μm thick disks. The disks were then mechanically polished to ~100μm thickness disks with 1μm surface finish using an Allied High Tech Multiprep polisher with water as lubricant. The thinned disks were electropolished using an electrolyte (HNO_3 (9%), butyl cellosolve + methanol mixture (1:2)) at a temperature between -42°C and -50°C, at 42 Volt using a Struers Tenupol electropolisher [63]. The current during the electropolishing stayed between 40 and 60mA. The thin regions of the BMG were usually covered with a thick but optically transparent layer of metal oxide. We later found that this thick oxide is actually induced by the water lubricant during the mechanical polishing. Such oxidation by water is much more severe than the naturally occurring air-induced oxidation, so for the future work, we recommend using water-free, oil based lubricants, such as Allied Blue-lube. In this work, we used a multi-step wet-etching method to remove the thick oxides [63]. The electropolished sample was first dipped and etched in 125°C phosphoric acid for 2 seconds, then cleaned in methanol for ~5 seconds, and etched again in HNO_3 for 2 seconds at room temperature. After that, the samples were cleaned again in methanol for about 10 seconds. The etching process in phosphoric acid

also involves oxidation of the surface, leaving a thick, reddish copper oxide on the surface of the sample. The copper oxide dissolves instantly in the HNO_3 in the next etching step. The wet-etching method is effective, but there are some side effects. First, the surface becomes rough and causes thickness variation, which may induce artifacts in $V(k)$. The artifacts caused by the thickness variation will be discussed in detail in section 2. 4. Second, since the phosphoric acid is viscous, some of it may not be washed off completely in the methanol cleaning process. The remaining acid layer may cause contamination problems in TEM, and it could also cause electron scattering and unwanted background in $V(k)$. Even after the wet-etching, the sample surface slightly oxidizes in the air before being inserted into the TEM vacuum, which is unavoidable.

The as-quenched ribbon BMG samples were already ~400μm thin, so they were used for electropolishing directly. Sample were either punched into 3mm disks or cut to ~3mm squares before electropolishing, and the same electropolishing conditions described above were used. For some samples, a low energy ion milling (Fischione 1040 Nanomill) [64] was used instead of wet-etching. 60x20μm^2 thin areas of the samples were focused and milled at 20° on both sides for 20 minutes each, at -168°C, at 700eV with a beam current of 115pA. The samples were then plasma cleaned at 20psi Ar + O_2 mixture for ~30 seconds. Low energy ion milling brings 3 positive effects to the samples, which are (i) removing hydrocarbons, (ii) removing surface oxides, and (iii) some degree of sample thinning. As a result, this method provides more uniformly clean and thin samples than the wet-etching, but slight air oxidation of sample after the low energy ion mill is still inevitable.

For FEM, the final BMG sample thickness needs to be only a few tens of nanometers, and it is the electropolishing that primarily decides the final thickness. The processes after the electropolishing, such as wet-etching or low energy ion mill, improve the surface condition but do not significantly change the sample thickness. Thin areas can be found at the edges of the holes made by electropolishing, but not every hole has thin areas that are thin enough. Electropolishing is a process that is difficult to control, and using same experimental parameter does not guarantee thin areas every time. In our experience, the thin areas were mostly found around the holes with high curvatures in their shapes. For example, small circular holes, typically ~50μm or less in diameter, have better chance to have thin areas than bigger circular holes. An ellipsoidal hole with high curvatures at both ends, even if the hole is big, also has a high chance of having thin areas at the ends. The position of the hole in a sample does not matter, although it is easier to detect the small holes at the center by the light sensor in the electropolisher than the holes at the edges. One important thing to notice in the BMG ribbon samples, however, is whether the hole was formed in a region that had been already thin as-quenched, because the region might have had a irregular quench rate [64]. This effect is discussed in detail in Chapter 3.

Some of the BMG samples were annealed to examine the effect of structural relaxation [63, 64]. The annealing temperature was typically set to about 85~87% of the T_g, except for the "reset" anneal which was performed slightly above T_g [38] for a few minutes [64]. Samples were annealed either in a furnace, or in a DSC by our collaborators, Melgarejo and Dr. Stone.

2. 2. FEM in CTEM

A CTEM instrument must meet several conditions in order to perform FEM. First, the physical size of OA must be very small, typically 10μm or less, to have R>1nm [47]. Second, the objective aperture must be placed exactly at the back focal plane of the electron ray path, which we found is not the case in some commercial TEM models optimized for HRTEM (*eg*. FEI CM200). Finally, hollow cone DF is preferred because it captures all diffraction in all angular direction in one k, but not required [47]. With hollow cone mode, the DF image at the detector is an angular averaged diffraction signal, so the magnitude of V becomes lower. Because of this, a direct comparison of absolute magnitudes between the V from hollow cone DF FEM and the V from tilt DF FEM is difficult.

The real space speckles of MRO in a DF image are best resolved at the exact focus, which maximizes V [47]. The exact focus was found by choosing a defocus that maximizes V in the image, among a series of DF images as a function of defocus. This focal series of V was taken before every $V(k)$ acquisition in a sample area [63, 65].

It is necessary to have enough electron counts in DF images to make V statistically reliable, but with a minimum beam exposure to the sample and a minimum acquisition time. High illumination convergence angles, between 2.0 to 4.0mrad, were chosen to have enough counts in a given exposure time, but at the expense of substantially reduced illumination coherence [63, 65]. The average CCD pixel count in an image was kept constant by steadily increasing the exposure time with increasing k, and a k range of 2.0 to 8.0nm^{-1} was chosen to cover the 1st and 2nd diffraction peak positions of the BMG. The number of k steps in a $V(k)$ was typically 18 to 20, and the acquisition of one $V(k)$ series took about 10 minutes. The size of MRO speckle in the DF images must be larger than a CCD pixel, so typically R~3 pixel length

was used. 2D selected area diffraction of the sample area was taken before and after each FEM acquisition to ensure no beam damage to the sample. Typically more than 10 $V(k)$'s were acquired from different areas of the samples, averaged, and reported with an uncertainty of the standard deviation of mean. DF images were post processed to remove the MTF and shot noise as described in [66].

2. 3. FEM in STEM

STEM FEM was performed in a C_s-corrected FEI Titan STEM operated at an acceleration voltage of 200kV [50, 64]. Previous STEM FEM experiments were performed in STEMs based on two main condenser lenses [49, 52], but the Titan has 3 main condenser lenses, so it has more flexibility in probe formation [50, 67]. We used the 'microprobe mode (μP-mode)' of the FEI control software for the Titan STEM. This mode allows wider range of Q, making it possible to form probes with large R up to 11nm, which is almost 3 times larger than the probes in previous STEM FEM experiments [50].

FEM resolution, R (nm)	C2 aperture diameter (μm)	Convergence half angle (mrad)	Spot number
0.8	10	1.91	7
1.3	10	1.2	7
2.0	10	0.74	7
3.5	10	0.43	6
5.0	10	0.3	6
11	5	0.14	4

Table 1. Probe conditions and exposure times for 6 different FEM resolutions. Exposure time was constant at 6 seconds [50].

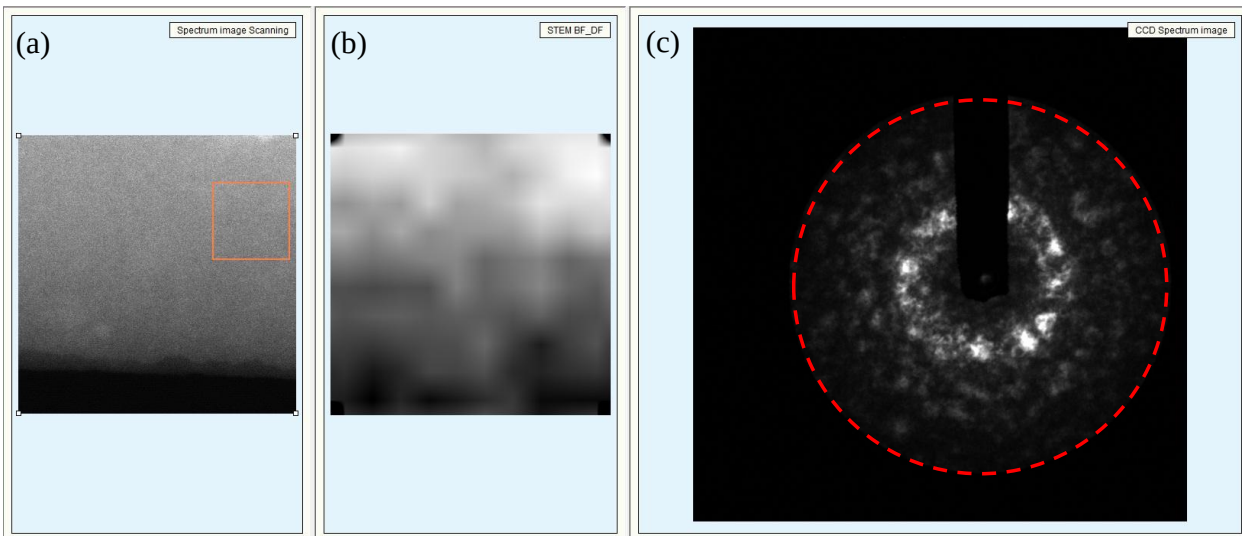

Figure 3. A typical FEM user interface during the data acquisition in FEI Titan. (a) An HAADF image of a sample area at 1.3Mx. The image is 150nm in length in both x and y directions, and the orange box indicates the area examined by FEM probes. (b) An HAADF image of the sample simultaneously acquired with the (c) FEM nanodiffraction from the area inside the orange box in (a). A 10 by 10 grid probe positions were used with R=1nm for this example. The red dashed circle indicates the GIF entrance aperture.

Six different probes sizes from 0.8 to 11nm were formed with the conditions summarized in Table 1 [50]. For reliable comparisons between the V's from different R's, the coherence length of each R must be constant [68]. Constant coherence can be achieved by constant probe current [67], so we changed the spot number accordingly (lower spot number has higher current) to compensate the change in current as the convergence angle changes, while the exposure time was kept constant at 6 seconds. Probes formed with each condition had well-defined Airy ring which is an indication of good coherence [67].

The probe was focused on the specimen using the Ronchigram. A camera length of 512mm in energy filtered STEM (EF-STEM) mode in Titan was chosen. The EF-STEM mode scales the camera length an order of magnitude longer so the CCD detector (a US1000 CCD in a GIF 865 image filter) can capture the nanodiffraction in a longer k range. A Gatan ADF detector

mounted on the 2.5mm GIF entrance aperture was inserted to collect HAADF images of the sample area simultaneously with the FEM nanodiffraction patterns, as shown in Figure 3. The GIF entrance aperture is smaller than the CCD area, so it appears as a circular rim in the nanodiffraction image (Figure 3(c)). With camera length of 512mm in EF-STEM mode, a pixel length is 0.0546nm^{-1}, and the maximum k is about 10nm^{-1} which is limited by the GIF entrance aperture. Both the convergence angle and the camera length had been calibrated using standard TEM samples before the FEM experiments. When a nanodiffraction pattern, which is in k-space, is focused on the detector plane, it should not move as the probe moves in real space, so we focused the diffraction pattern on the detector by minimizing the motion of the diffraction pattern while scanning the probe in an area at 1.3Mx. The diffraction focus was adjusted by manually changing the diffraction lens (the first projector lens) current using the FEI free-lens control interface. The zero beam of the nanodiffraction pattern must be blocked to prevent CCD damage, but the factory made beam stop in Titan was too big, so we customized a beam stop with a focused ion beam and used it for FEM. The selected sample area must be large enough so that two adjacent probe positions do not overlap. GIF energy filtering was used with a slit width of 10eV to remove the inelastically scattered electrons. Typically 10 by 10 probe position grid was used, and 512 by 512 pixel nanodiffraction patterns were acquired with CCD binning of 4, as shown in Figure 3. The specimen drift during 6 second exposure was typically smaller than ~5% of R in all conditions. To reduce shot noise contribution to the V [66, 69], the peak intensity at the 2nd diffraction peak was kept over minimum 500 counts in each $I(k)$. The gain of CCD is 4.72, so this corresponds to 106 detected fast electrons. For each resolution, $V(k)$'s from typically ~10 different areas were acquired, and later averaged.

The nanodiffraction patterns in .SER format files were loaded in Wavemetrics Igor software for further analysis. $I(k)$s were calculated from each nanodiffraction and $V(k)$ was calculated using Eq. 1. The variation of sample thickness may cause unwanted background in V, so thickness filtering is necessary. The methods for measurement and filtering of sample thickness are discussed in section 2. 4. $V(k)$'s from different areas were averaged and reported with a uncertainty of one standard deviation of the mean (SDOM). The shot noise contribution was subtracted from the data as described in Fan et al. [69].

2. 4. Sample thickness measurement and thickness filtering of STEM FEM data

FEM must be performed on relatively thin samples for two reasons. First, V is inversely proportional to the sample thickness, t, so thin samples maximize V [51, 68]. Second, FEM simulations, such as FEMSIM [70], use the kinematic diffraction approximation which is only valid in a thin sample in real experiments, so the comparison between experiment and simulation becomes better with a small t. If the t is too small, however, there will be not enough electron scattering on the detector, so there is an optimum thickness. We use the elastic electron transmittance (T), as a measure of sample thickness [71]. For amorphous specimens, elastic scattering obeys Poisson scattering statistics depending on the elastic mean free path, Λ_{BF} [71],

$$T = \exp\left(\frac{-t}{\Lambda_{BF}}\right). \qquad \text{(Eq. 6)}$$

We measured Λ_{BF} using the method described in Schweiss et al. [72], and found that the Λ_{BF} of $Zr_{50}Cu_{45}Al_5$ is 39±1nm and the Λ_{BF} of $Cu_{64.5}Zr_{35.5}$ is 45±4nm. This T method is analogous to the more common method using EELS and the inelastic mean free path, but we prefer this method in

FEM because the elastic scattering events are more common in thin samples, and because it can be used more easily without switching to the EELS mode. For thin film Si samples, the areas with T~70% were chosen for FEM [73]. However, in BMG systems where average atom numbers are much higher, T~70% requires the sample to be about ~15nm thick, which is difficult to make consistently over large areas. In addition, there is always a thin oxide layer on the surface of BMG, which also slightly reduces the T. So in STEM FEM with BMG, we chose T~50% as a standard, which, for example, corresponds to t~27nm in case of $Zr_{50}Cu_{45}Al_5$ BMG.

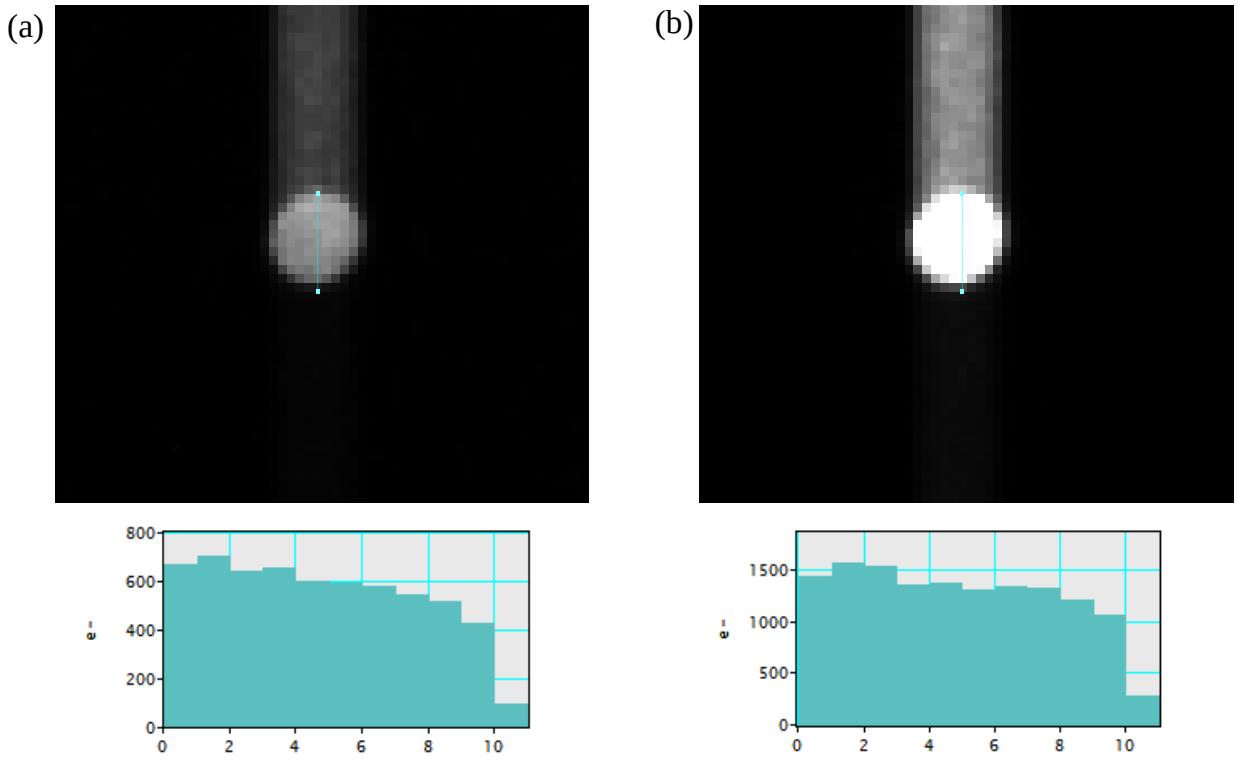

Figure 4. Zero beam images (above) and intensity line profiles of a STEM probe from (a) a sample area, and (b) a hole. The vertical streaks are artifacts from the microscope shuttering at very short exposure time.

In STEM, the *T* of a sample is the ratio between the zero beam intensity of diffraction patterns with and without the sample. Figure 4 shows the zero beam images and the intensity line profiles of a STEM probe from (a) a sample area and (b) a hole. We used the maximum values at each intensity profile to calculate the intensity ratio. In this example, the *T*~700/1,500=46.7%. We later found that using the maximum value at the intensity profile may cause a slight error in *T* because of the electron beam broadening inside the sample. The beam broadening effect changes when *R* changes, so the *T*'s measured by two probes with different *R* can be different, for example, by up to a few percent between *R*=2 and 11nm cases. For future works, we recommend to compare the integrated intensity inside the zero beam instead of the maxima for a better accuracy, although it would be technically more difficult.

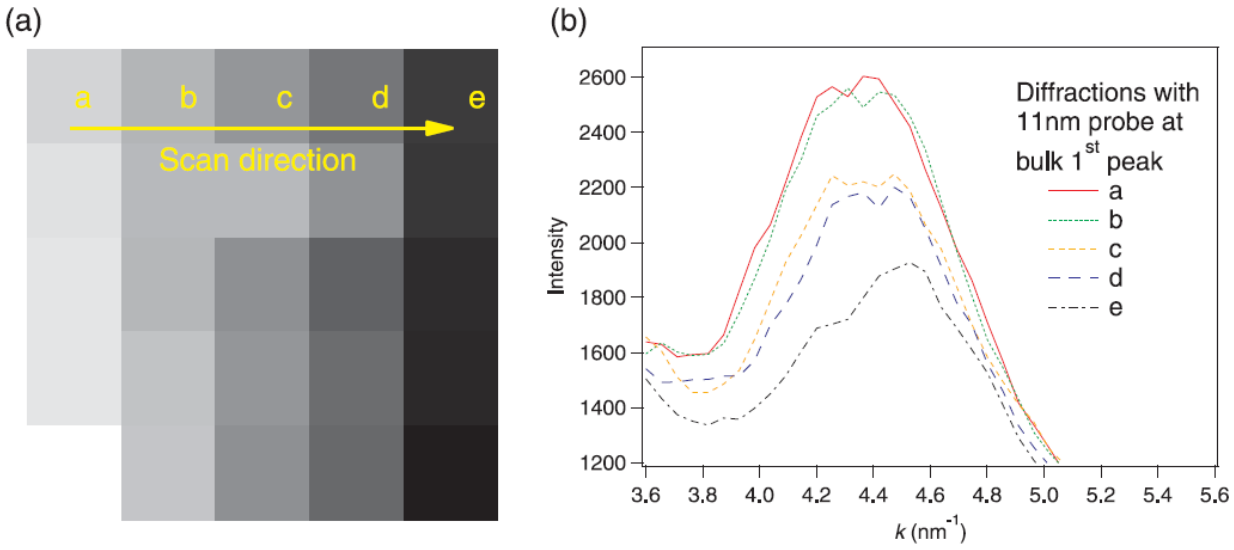

Figure 5. (a) HAADF image taken simultaneously with the FEM nanodiffraction acquisition. The arrow indicates the scan direction, and the regions (a-e) indicate locations of the probe. (b) Annular averaged diffraction intensities (*I*(*k*)s) from sample areas (a-e) in the HAADF image in (a). The gray scale in (a) extends from 6,203 to 7,027, with detector offset of 4,399 counts [50].

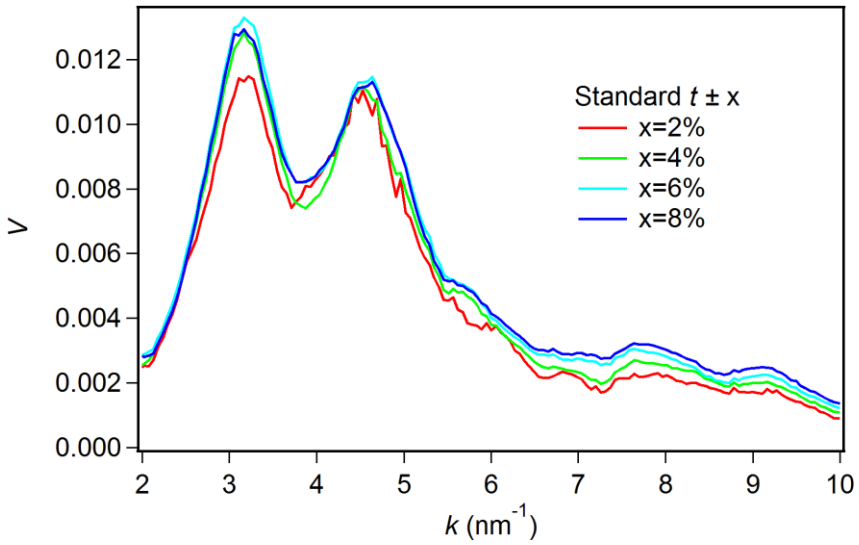

Figure 6. $V(k)$ from $Cu_{64.5}Zr_{35.5}$ with different thickness filtering limits, t±2, 4, 6, and 8%. Error bars are omitted for clarity.

Even with a standard t set in a FEM experiment, there are always small thickness variations caused by the sample shape and the roughness of the surface. The variations in sample thickness cause artifacts in V because I depends on the mass of the material, as shown in Figure 5. We found that this effect can dominate the structure-induced V [50]. To remove this effect, we have developed a thickness filtering method based on a HAADF image acquired simultaneously with the STEM FEM nanodiffraction [50]. For a chemically homogeneous amorphous material, the HAADF image intensity is a linear measure of the specimen thickness. The HAADF image of an area with measured T=50% area provides a calibration point among the images, and the nanodiffraction patterns from the areas with similar HAADF intensities were chosen for V calculation. Typically, the areas with standard t±0.5nm were used. If we set only one standard t in an experiment, however, we only get to use a small portion of the nanodiffraction data because the thickness variation in a typical STEM FEM series is about ±3nm. To include more data in the V calculation, we later used 5 different standard t's in the T

range of 50±2%, calculated the V's for each standard t [64]. V is inversely proportional to t [51], but in the given T range this effect appeared to be very small [64], so averaging the V's from different standard t's is acceptable. Because of this thickness filtering, we get 5 V's for each standard t's from one FEM series, and the V's from multiple FEM series were averaged all together and reported with a uncertainty of one SDOM. Figure 6 shows the effect of the thickness filtering to $V(k)$. $V(k)$ gradually increases throughout all k range as the filtering limit increases, so the thickness variation in the sample must have affected the data.

2. 5. Electron $G(r)$

Electron $G(r)$ was measured in a Zeiss 912 TEM with in-column Ω energy filter operated at 120kV using techniques and software developed by A. M. Clausen [65]. The energy filtered electron diffraction patterns were taken with the incident beam tilted off axis to reach the maximum possible k through the energy filter, and recorded on high dynamic range Ditabis image plates. The zero beam was fit to a pseudo-Voigt function [74] and subtracted from the diffraction pattern to obtain $I(k)$. $I(k)$ was fit to the Kirkland electron scattering factors [75] to find the reduced intensity function, $\varphi(k)$, and its Fourier transform, $G(r)$, as described by Cockayne et al. [76].

Chapter 3. FEM Experimental Results

In this chapter, we report experimental FEM results from 3 different BMGs: CTEM FEM of cast $Zr_{54}Cu_{38}Al_8$ [63], STEM FEM of melt-spun $Cu_{64.5}Zr_{35.5}$ [50], and STEM FEM of $Zr_{50}Cu_{45}Al_5$ [64]. The $Zr_{54}Cu_{38}Al_8$ and $Zr_{50}Cu_{45}Al_5$ BMGs were annealed in different conditions to observe the effect of structural relaxation on nanoscale MRO.

3. 1. Experimental details

BMG samples cut from top and bottom of the ingots were examined using XRD (Siemens Hi-star 2D) to check overall quality, including the absence of crystal peaks, before the FEM experiments [63]. The T_g of this same BMG was found using DSC by our collaborators [63, 64]. The $Zr_{54}Cu_{38}Al_8$ ingot was annealed in a furnace at 315°C ($0.87T_g$) for 24 hours, and the $Zr_{50}Cu_{45}Al_5$ ribbons were annealed at 300°C ($0.85T_g$) for 10 and 60 minutes, and at 435°C ($1.06T_g$) for 2 minutes. In a $Zr_{50}Cu_{45}Al_5$ ribbon, we found a "trench" region accidentally formed on the surface at the time of quenching. The trench was formed in both sides of the ribbon, so it was not in contact with the spinning wheel, therefore the quenching rate of this region must have been different than the other normal regions, although we are not sure if the rate was faster or slower. The structure in this more abnormally quenched trench region was also investigated.

After electropolishing, the surface oxides on the $Zr_{54}Cu_{38}Al_8$ and $Cu_{64.5}Zr_{35.5}$ BMGs were removed by wet-etching, and the oxide on the $Zr_{50}Cu_{45}Al_5$ was removed by low energy ion milling. A JEOL 4000EX TEM operated at 200kV was used for CTEM FEM of $Zr_{54}Cu_{38}Al_8$ BMG ingot samples at R=1.0nm [63, 65]. 300 x 300 pixel tilted DF images were acquired using

a Gatan MSC 794 CCD camera. One FEM acquisition series consists of 18 DF images from k = 2.0 to 8.6nm^{-1} in equal intervals. 10 data series from different areas of several TEM specimens were acquired from the as-cast and annealed material. The $V(k)$ data is the mean of those ten areas, presented with one standard deviation of the mean error bars. Images were processed with a band-pass Fourier filter from 0.06 to 0.6nm^{-1} in image spatial frequency.

STEM FEM was performed in a C_s-corrected FEI Titan STEM operated at acceleration voltage of 200kV for $Cu_{64.5}Zr_{35.5}$ and $Zr_{50}Cu_{45}Al_5$ BMG ribbons [50, 64]. For $Cu_{64.5}Zr_{35.5}$ BMG, six different R's from 0.8 to 11nm were used, and the data were processed with thickness filtering with a standard t=26±0.5nm. For $Zr_{50}Cu_{45}Al_5$, R=2, 4, and 10nm were used. 6 different standard t's between 24.8 and 29nm were chosen, and all 6 V's calculated for each standard t±0.5nm were averaged.

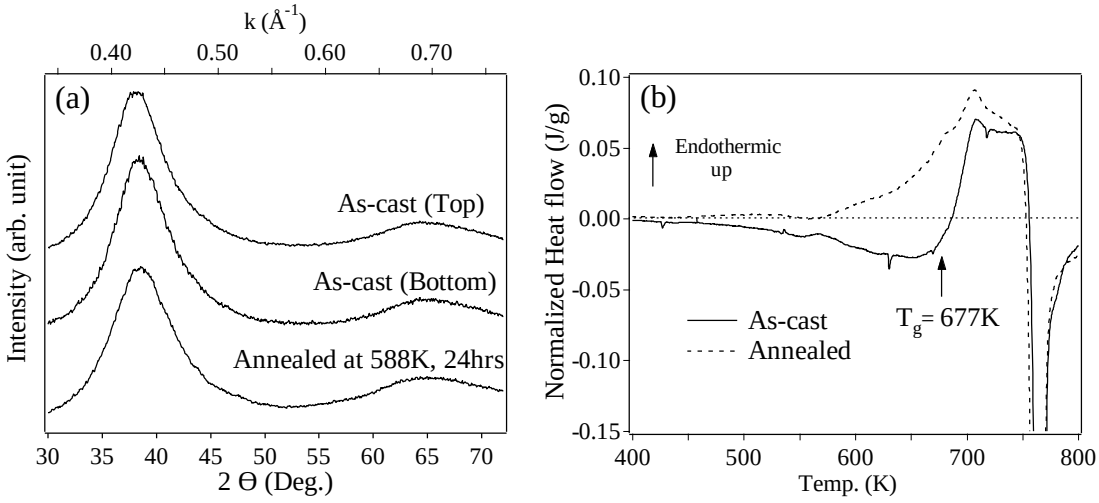

Figure 7. (a)XRD, and (b) DSC data from as-cast and annealed $Zr_{54}Cu_{38}Al_8$ BMGs [63].

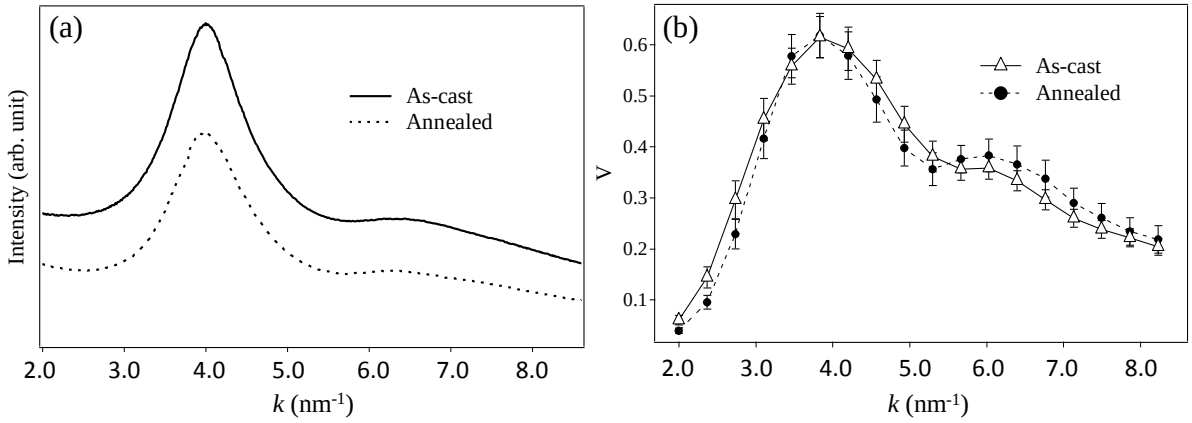

Figure 8. (a) $I(k)$'s by energy filtered diffraction, and (b) FEM $V(k)$'s from as-cast and annealed $Zr_{54}Cu_{38}Al_8$ BMG [63].

3. 2. Results

3. 2. 1. CTEM FEM of $Zr_{54}Cu_{38}Al_8$ BMG

Figure 7(a) shows x-ray diffraction data from as-cast and annealed $Zr_{54}Cu_{38}Al_8$ show that the as-cast ingot is fully amorphous from top to bottom, and there was no detectable change by the sub-T_g annealing [63]. The DSC data in Figure 7(b), however, shows that the exothermic peak at ~650K (377°C) in the as-cast material disappeared after the annealing. The exothermic peak indicates the structural relaxation during the DSC annealing, and its absence in the annealed data means that the annealed sample has been structurally relaxed by the sub-T_g annealing before the DSC measurement.

Figure 8(a) shows the energy filtered electron diffraction $I(k)$'s from as-cast and annealed $Zr_{54}Cu_{38}Al_8$ BMGs [63]. Like XRD data, electron diffraction did not show any detectable change after the annealing, which means that the SRO in BMG was largely unaffected by the structural relaxation. Figure 8(b) shows the $V(k)$'s from as-cast and annealed $Zr_{54}Cu_{38}Al_8$

BMGs. The peaks at k=4.0 and 6.0nm^{-1} in the $V(k)$ show that there is measurable MRO in this BMG at 1nm spatial resolution. However, there was no statistically significant difference outside error bars between the $V(k)$'s of the as-cast and annealed samples. The structural relaxation seen in the DSC data must have involved some change in the atomic structure, but neither the $I(k)$ nor the $V(k)$ detected the change. Since R=1nm in this FEM experiment, this means that the structure at <1nm scale were unchanged by the structural relaxation, and the change in structure might have occurred at a length scale longer than 1nm. STEM FEM experiments on different samples at R=2nm discussed in section 3. 2. 3 support this hypothesis. It is also possible that there might be a structural change smaller than the detection limit of this experiment. As discussed in section 1. 2, CTEM FEM has low probe coherence and low k sampling, so small changes in detail peak position or magnitude might not be captured in this experiment. RMC modeling of this data set is discussed in section 4. 3. 1.

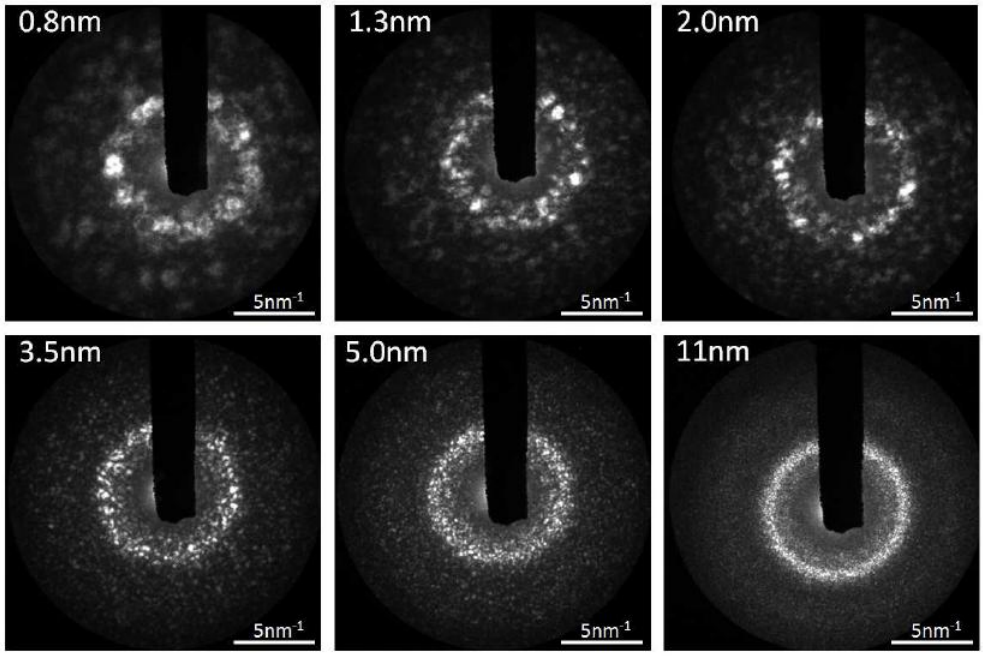

Figure 9. Example nanodiffraction patterns from $Cu_{64.5}Zr_{35.5}$ using six different probe sizes (R's) [50].

3. 2. 2. VRFEM of $Cu_{64.5}Zr_{35.5}$ in STEM FEM

Figure 9 shows example nanodiffraction patterns from different areas of $Cu_{64.5}Zr_{35.5}$ BMG at different *R*'s [50]. The number of speckles increases when *R* becomes larger, because more MRO units are involved in diffraction with larger probes. The diameter of the speckles is proportional to *Q* and inversely proportional to *R*. With smaller *R*'s (~2nm or smaller), the speckles are big, because of the larger convergence angle. With larger *R*'s (3.5nm or larger), the speckles are smaller and the pattern becomes closer to an amorphous diffuse ring pattern. Some of the nanodiffraction patterns also appear to have some rotational symmetry, detailed analysis of which are discussed in Chapter 5.

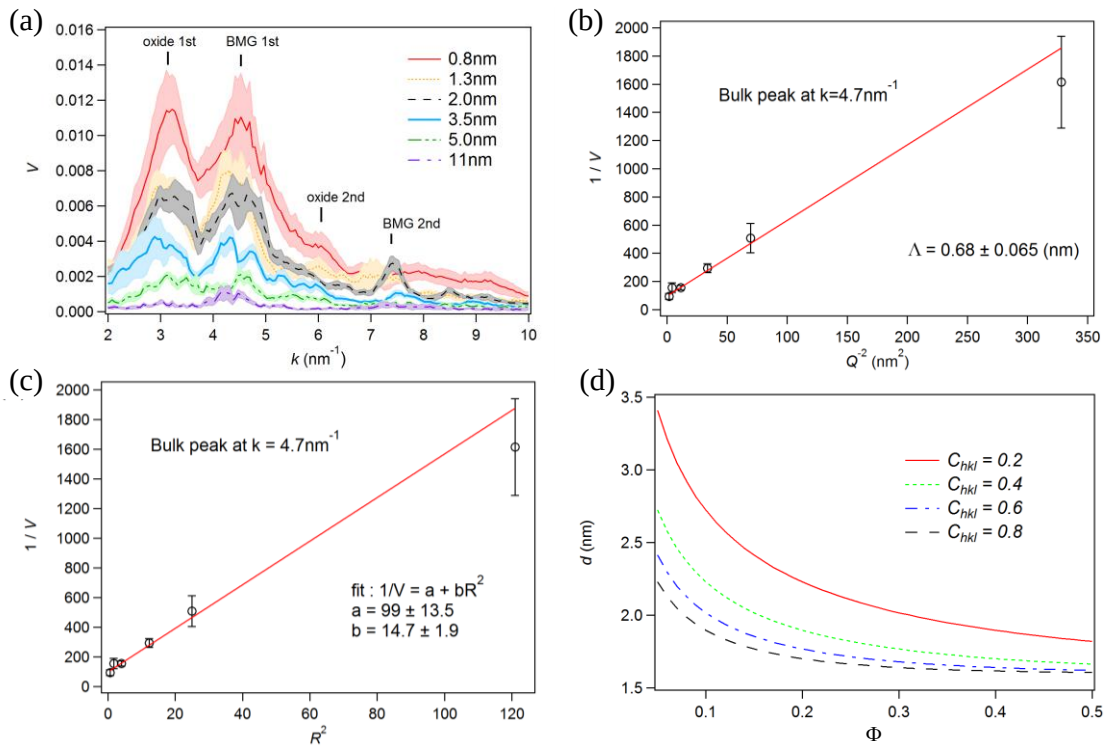

Figure 10. (a) $V(k)$ plots of six different *R*. Solid lines are averages, and colored bands indicate the uncertainty range (standard deviation of mean). (b) $1/V$ versus $1/Q^2$ and (c)$1/V$ vs. R^2 for bulk 1st peak in (a). The circles are the data points, and the error bar is the standard deviation of the mean. Lines are linear fits to the data points. (d) MRO size *d* versus volume fraction Φ calculated from VRFEM data using amorphous / nanocrystal composite model [50].

Figure 10(a) shows the $V(k)$'s from the nanodiffraction of $Cu_{64.5}Zr_{35.5}$ using 6 different R's [50]. The peaks for the bulk BMG and the surface oxide are indicated in the panel. The data show that the structural fluctuation in this BMG is high at ~1nm scale, but the fluctuation gradually decreases as the R increases. At 11nm scale, the structural fluctuations become nearly zero, which means the structure at or over ~11nm is almost homogeneous. Surface oxide peaks, identified by their smaller interatomic spacing and lower k, also showed similar behavior. Two models, the pair persistent model [48] and the amorphous / nanocrystal composite model [51] (section 1. 2, Eqs. 2-5), were applied to calculate Λ and d. Figure 10(b) shows the linear fit to the $1/V$ vs. $1/Q^2$, from which Λ=0.68±0.07nm. The linear fit to $1/V$ vs. R^2 is shown in Figure 10(c). The d vs. Φ relationship was calculated using Eq. 6 and the parameters, t=26nm, Ω=0.0385nm^2, and ρ=57.05 atoms/nm^3, and shown in Figure 10(d). C_{hkl} is not known for this system, so the d vs. Φ is shown for a possible range of C_{hkl}. The plot shows that the d is likely between 1.7nm and 3.0nm. Gibson argued that the Λ can be converted to a characteristic width of MRO, W, through $\Lambda^2=W^2/10$ [48], so in this case W~2.2nm which is within the range of d.

The $V(k)$ data in Figure 10(a) also provides some intuitive understanding about the types of MRO in the BMG. The BMG 1st peak in $V(k)$ has two divided maxima which do not exist in $I(k)$, especially in the R=3.5nm data. The 2nd maximum at k~4.7nm^{-1} approximately matches the inverse of the FCC Cu {111} spacing of 0.209nm. The 1st maximum at k~4.3nm^{-1} is likely related to the interplanar spacing in a Cu-Zr MRO, based on comparison to plane spacings in various intermetallic alloys. The distinction between the two maxima disappears in $V(k)$'s with smaller R's where the reciprocal space resolution is worse. There may be a small shoulder peak at k~3.9nm^{-1}, which is inverse of the HCP Zr {0002} spacing of 0.257nm. This suggests that the $V(k)$ signal may be related to the plane-like MRO in the material. This is similar to the

conclusion from our RMC simulation results which are discussed in Chapter 4. This plane-like order is perhaps related to the 'critical-like' order seen in recent simulations on glass forming liquids [35, 36]. The icosahedral MRO [31], if exists, can generate peaks in $V(k)$ [65], but it is difficult to confirm which peak it might correspond to in this data set. More insights on the icosahedral MRO are discussed in Chapter 4.

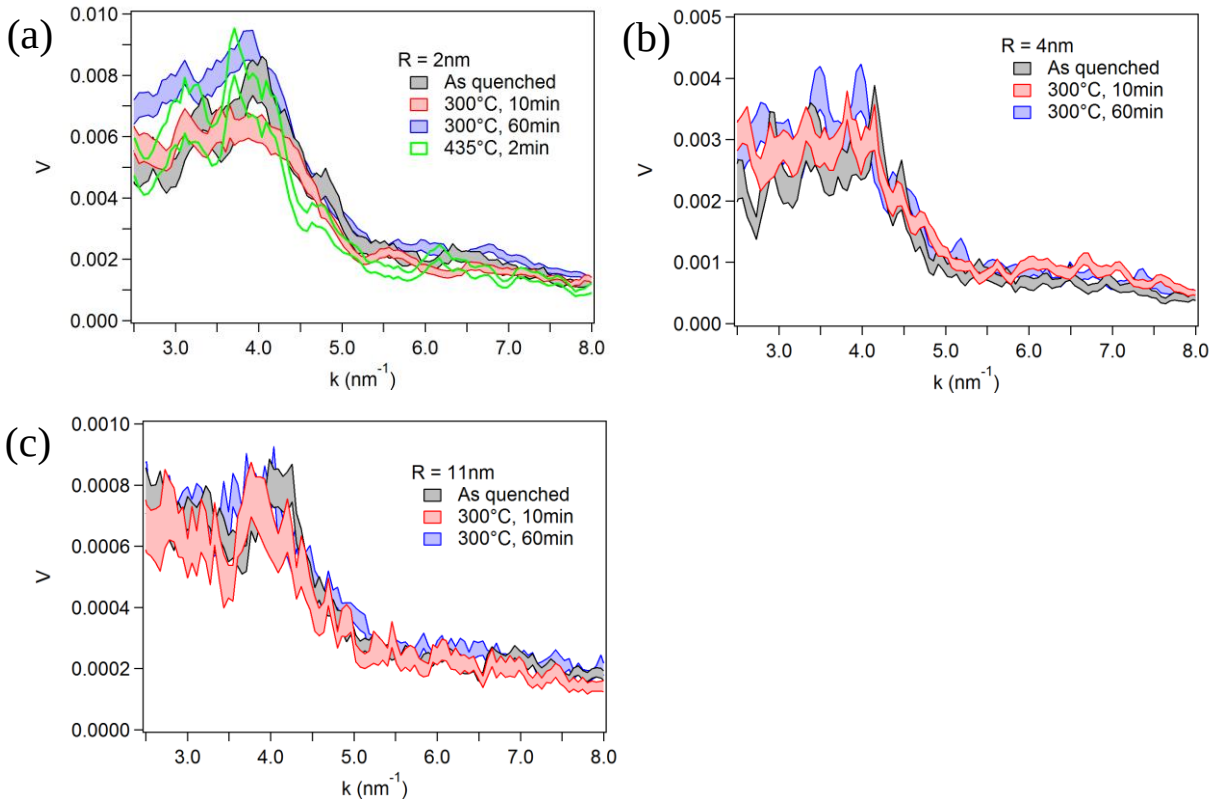

Figure 11. VRFEM data with R=2, 4, and 11nm probes for $Zr_{50}Cu_{45}Al_5$ BMG as-quenched and annealed in different conditions. The data were presented as bands which represent the uncertainty (SDOM) range. The sample annealed at 435°C for 2 minutes was only examined with R=2nm probe [64].

3. 2. 3. $Zr_{50}Cu_{45}Al_5$ STEM FEM

Figure 11 shows the VRFEM data from the as-quenched and the annealed $Zr_{50}Cu_{45}Al_5$ BMG samples using R= (a) 2, (b) 4, and (c) 11nm [64]. The sample annealed at 435°C for 2 minutes was examined only with R=2nm. In Figure 11(a), the $V(k)$ from as-quenched sample showed peak maximum at k~4.0nm^{-1}, while the $Cu_{64.5}Zr_{35.5}$ BMG showed a maximum at ~4.3nm^{-1} in Figure 10(a). This suggests that the dominant types of MRO may be different in the two BMGs, and this is also perhaps related to the difference in their GFA. $V(k)$ peaks at a smaller k means that the interplanar spacing of the corresponding MRO is larger, so the $Zr_{50}Cu_{45}Al_5$ have MRO that has a larger interplanar spacing. This is reasonable because the ternary glass has more Zr atoms, which are bigger than Cu atoms. As mentioned in the previous section, the peak at k~4.7nm^{-1} may be related to the FCC Cu-like MRO, and this peak is also present in the $Zr_{50}Cu_{45}Al_5$ data, but as a small shoulder peak. When the sample was annealed at 300°C for 10 minutes, the peaks near k~4.0 and 4.7nm^{-1} decreased, but the peaks increased again when the sample was annealed for 60 minutes. Compared to the as-quenched data, however, the maximum peak of 300°C, 60 minute data have shifted to lower k region, suggesting a possible change in types of MRO. Finally, the data from the reset annealing at 435°C (1.06T_g) for 2 minutes showed a clear peak shift from the as-quenched data, as the peak at k~4.0nm^{-1} decreased and the peak at k~3.7nm^{-1} increased. The reset annealing must have almost fully relaxed the structure because the DSC data showed no exothermic peak [37, 77], so the maximum peak in $V(k)$ gradually shifted from k~4.0nm^{-1} to 3.7nm^{-1} as the degree of relaxation increases. The structural change of BMG detected in $V(k)$ by annealing is larger than any other pervious diffraction measurements [*eg.* 39]. The R=4nm and 11nm data in Figure 11 (b) and (c) also

show similar trend, but not as clearly as the *R*=2nm data. This suggests that the structural change by annealing mostly occurred in a length scale close to 2nm.

Knowing the details of the structural change by annealing is important, but not easy. The pair persistent model only provides size information of MRO. For the MRO type information, we still have to depend on direct interpretation of *k* peak positions in *V*(*k*), which is difficult in this case. The pair persistent model also assumes only one type of MRO, while BMG must have multiple types of MRO, based on the multiple sub peak positions in *V*(*k*). The amorphous / nanocrystal composite model involves more structural information, but shares the same limitations as the pair persistent model, while demanding even more *a priori* information about the type of MRO. Therefore, we used H-RMC simulation for the interpretation of the data in Figure 11, which is discussed in Chapter 4.

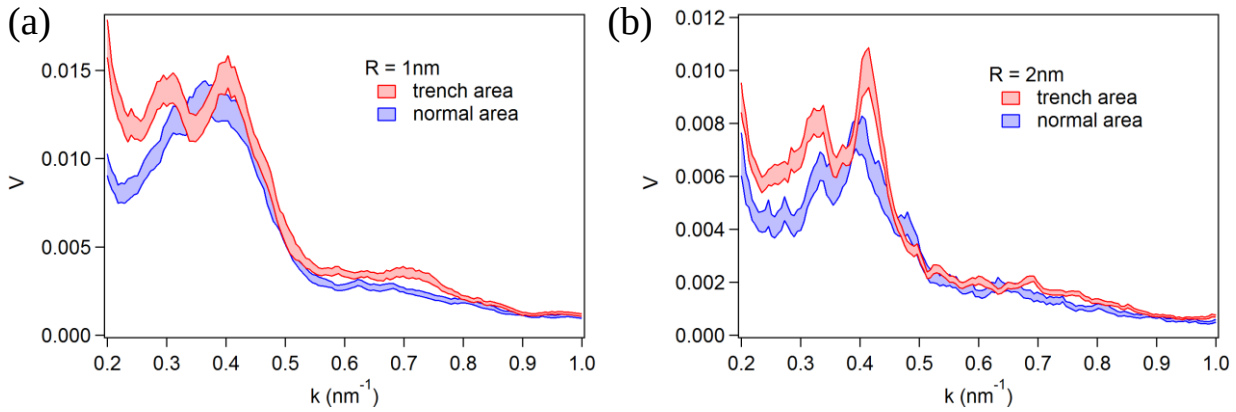

Figure 12. VRFEM data with *R*=1, and 2nm probes for normal and trench regions of $Zr_{50}Cu_{45}Al_5$ BMG sample.

Figure 12 shows the $V(k)$ acquired from the abnormally quenched trench area of the $Zr_{50}Cu_{45}Al_5$ sample, using (a) R=1nm, and (b) 2nm, compared to the data acquired from normally quenched areas. The data shows that the $V(k)$ from the trench sample has elevated peak at k~4.2nm^{-1} in both R=1 and 2nm data. This result shows that quenching rate of the BMG can also significantly effect the MRO structure. However, since we do not know whether this change in $V(k)$ was due to a faster or a slower quenching, the detail mechanism of how the quenching rate affects the MRO structure remains unclear.

Chapter 4. RMC and H-RMC

4. 1. Introduction

We used RMC simulation incorporating FEM data to study the detailed atomic structure of MRO in BMG [64, 65]. The type of MRO can be determined by the internal structure of the MRO regions in the model, which particularly interesting in BMGs because there may be more than one type of MRO. The *k* peak positions in *V*(*k*) are related to the internal structure of MRO, and previous FEM work has used hand-made or MD generated atomic models to match the simulated *V*(*k*) peaks to the peaks in the experimental *V*(*k*) [59, 78]. However, in multi-component systems like BMGs, this is difficult because there are many possible atomic configurations that generate peaks near the same *k*.

RMC simulation generates an atomic model which matches the experimental data [79]. Unlike in a typical Monte Carlo (MC) simulation which minimizes the system energy, RMC minimizes the χ^2 deviation between the experimental and simulated data [79].

$$\chi^2 = \sum_i \frac{\left(experiment(i) - simulation(i)\right)^2}{\left(uncertainty(i)\right)^2}, \qquad \text{(Eq. 7)}$$

where *i* is the number of data points. Minimizing the χ^2 by MC moves can yield an output configuration which shows the best possible agreement with the experimental data [79-84]. Keen and Mcgreevy [79] first performed RMC refinement of amorphous SiO_2 against the *S*(*k*) from neutron diffraction, and the model quantitatively matched physical properties, such as bond angle distributions. However, even if there is a perfect match between the model and the data,

RMC can generate many different structures, all consistent with the same experimental data [81]. This problem of uniqueness is especially severe when the material (and model) lacks crystalline order, and when only one type of experimental data, typically g_2, is used in the simulation [81]. The uniqueness of model can be increased by including *a priori* knowledge of the material, and by including additional experimental data, such as EXAFS, with a proper weighting between different experimental data [79, 80]. There have also been attempts to combine RMC and conventional MC or MD simulations. H-RMC, a combination of Metropolis MC and RMC, was first tried by Opletal et al. [82], by combining the system energy by an interatomic potential and the χ^2 into one cost function. Experimentally constrained molecular relaxation (ECMR) combines RMC and 1st principle calculation by alternately relaxing a model between the two methods [83, 84]. Amorphous semiconductor models relaxed with ECMR match the experimental electron and vibrational density of states, while the models relaxed only with RMC do not [83, 84].

The use of $V(k)$ in RMC along with other data increases the uniqueness of the model, especially in MRO scale [83, 85]. Biswas et al. first performed RMC against experimental $V(k)$ from amorphous Si and found that RMC made nano-sized grains of ordered regions in the model that generates FEM signal [85]. Using a modified version of the FEM RMC code written by Biswas et al., we performed a RMC of a ternary Zr-Cu-Al BMG against electron $G(r)$ and $V(k)$ [65]. We also developed a H-RMC simulation that includes an EAM interatomic potential for Zr-Cu-Al and FEM $V(k)$, so the model can be more realistically confined from SRO to MRO scale [64]. The total χ^2 in our H-RMC is [64],

$$\chi^2 = EAM\ energy + \gamma \sum_i \left(s \cdot V(k)_{ex} - V(k)_{cal} \right)^2 / \sigma_i^2. \qquad \text{(Eq. 8)}$$

where γ is the weight of experimental $V(k)$, s is a scaling factor between experiment and simulation for $V(k)$, and σ is the experimental uncertainty. A synchrotron XRD $G(r)$, provided by our collaborators, Drs. Kalay and Kramer [86], was included in the total χ^2 in some H-RMC simulations, but here we presented data from the H-RMC with EAM potential and $V(k)$ data only.

4. 2. Simulation details

We first used RMC simulation against the electron $G(r)$ and $V(k)$ data from $Zr_{54}Cu_{38}Al_8$ BMG [65] with a RMC code based on the code written by Biswas et al. [81]. A model with dense random packed (DRP) 54,650 atoms of $Zr_{54}Cu_{38}Al_8$ in a 10nm cubic box at the experimentally determined density (ρ_0=6.82±0.04 g/cm^3, [87]) generated by MC minimization of a Lennard-Jones (LJ) potential was used as a starting configuration. The $G(r)$ was simulated by [65],

$$G_{cal}(r) = \frac{1}{r}\sum_i \sum_j \left[K_{ij} \cdot \delta\left(r - r_{ij}\right)\right] - 4\pi r \rho_0, \qquad \text{(Eq. 9)}$$

where K_{ij} is the electron scattering power of each type of pairs, i and j.

The $V(k)$ in RMC is calculated from simulated nanodiffraction intensities from the atomic model. Full dynamic diffraction simulations, such as Bloch wave simulation [88] or multislice simulation [75], are the most accurate, but they are computationally expensive and not suitable for RMC, which requires a FEM calculation in every MC step. For a faster calculation in RMC, we used a program called FEMSIM, which simulates FEM DF images of an atomic model to calculate V [70]. One simulated image is comprised of many pixels, the size of which is the FEM resolution. Kinematic scattering with a flat Ewald sphere is assumed for computational

efficiency, so the I of one pixel depends on the projection of the atomic structure in the column to the pixel [70],

$$I(\mathbf{r},k,Q)=\int_{r'} g_{2A}(r',\mathbf{r},Q)\,J_0(2\pi kr')\,dr'. \qquad \text{(Eq. 10)}$$

J_0 is zeroth-order Bessel function, and g_{2A} is the weighted, local 2D pair distribution function that is given by [70],

$$g_{2A}(r',\mathbf{r},Q)=\sum_j\sum_i f_i f_j A\left(2\pi Q\left|r-r_j\right|\right)A\left(2\pi Q\left|r-r_i\right|\right)\delta\left(\left|r_i-r_j\right|-r'\right), \qquad \text{(Eq. 11)}$$

where the f is the electron scattering factor, which is a function of k, A is the microscope point spread function, which is approximately an Airy function, and $r'\leq R$. Since the structure of amorphous materials is isotropic, one atomic model is rotated to many orientations, and one DF image is simulated per orientation. The total number of pixels, N, is the number of pixels per image multiplied by the number of orientations. V of all the I's is calculated from [65]

$$\begin{aligned}\left\langle I(k)\right\rangle &= \frac{1}{N_I}\sum_{i=1}^{N_I} I_i(k),\\ \left\langle I^2(k)\right\rangle &= \frac{1}{N_I}\sum_{i=1}^{N_I} I_i^2(k),\end{aligned} \qquad \text{(Eq. 12)}$$

and Eq. 1. In this simulation, we used 3 different orientations, parallel to the x, y, and z axes of the model. One simulated image contained 8 by 8 pixels, so N=192 in this simulation. The shape of a pixel needed to be circular because the intensity of a pixel was essentially limited by a projection of the A, which is a circle. The edges of the adjacent circular pixels were overlapped so that every atom position was included in the $I(k)$ calculation.

The magnitude of experimental $V(k)$ from CTEM FEM is much lower than the simulated $V(k)$ because of the relatively poor coherence of the measurement [49, 89], and because of the

thickness difference between the experiment (~20nm) and the simulation (10nm) [50]. We estimated that the scaling factor, *s* in Eq. 8, which accounts for these effects is ~2 in this case [65]. We did not use a combined cost function, such as Eq. 8, in this RMC, but instead we used an alternate RMC runs against each experimental data set, along with a step-wise quenching scheme until the χ^2 against both data sets was acceptably small. Maximum move distance of an atom was gradually decreased as temperature decreased. Since no interatomic potential was used in RMC, the bonding distances were limited by hard sphere cutoffs. To observe the effect of adding $V(k)$, a RMC simulation against only $G(r)$ was performed, and results were compared to the RMC against both $G(r)$ and $V(k)$. A fair convergence of χ^2 was achieved in approximately 1.5×10^7 MC steps. Running on a single processor, these simulations took about 7 days.

Later, we have developed an H-RMC code based on our experience from the FEM RMC [64, 90]. H-RMC was greatly improved in many different aspects. First, it combines RMC and an EAM interatomic potential developed for the Zr-Cu-Al system by Cheng et al. [22], so both chemical and diffraction information are applied to the model. Second, a significant speed-up was achieved by using a more efficient 'hutch-based' algorithm [91], and a computational parallelization by the message passing interface (MPI). Increase in computational speed allowed us to simulate $V(k)$ using up to 208 different orientations, so the isotropy of the output model greatly increased. The orientations were uniformly distributed in all spherical directions using Euler rotations, and the angle between two nearest orientations was 9°. Since the intensity is calculated from the x-y projection of the atom positions, the images from the orientations in upper hemisphere ($z \geq 0$) are same as the images from the orientations in the lower hemisphere ($z < 0$), so only the orientations in the upper hemisphere were considered. Unlike the previous RMC [65], we used square pixels with no overlap in this simulation because we found that the

overlap of pixels may cause artifact in $V(k)$, particularly in low k region. The use of square pixels, however, causes some error in the $I(k)$ calculation because the square pixel, inscribed in the circular projection of A, misses some atoms at the tail portion of the A. However, the error appeared to be small.

The use of EAM potential also contributed to the 3D isotropy of the refined models. $G(r)$ is a 1D quantity by its definition, and the simulated $V(k)$ is essentially a 2D quantity due to the flat Ewald sphere approximation [65], although this limitation is somewhat overcome by the use of many orientations. The EAM potential applies to the atomic bonding in any 3D direction, so it adds a pure 3D quantity to the model. The EAM potential also has crucial chemical information equivalent to the partial $G(r)$'s, which the experimental total $G(r)$ only weakly represents. In addition, our H-RMC refinement is also improved by the use of STEM FEM data which has higher quality than the CTEM FEM. STEM FEM has a high probe coherence which is comparable to the simulation, so only the thickness differences between the simulation and the experiment needs to be scaled for the $V(k)$ fitting. It also offers a lot more k points, although only 32 of 63 points in the k range of 3.5-7.0nm^{-1} were used for the refinement. The computation time is linear in the number of k points, so the reduced number of k points was selected to reduce computation time.

H-RMC simulations using the $V(k)$'s from $Zr_{50}Cu_{45}Al_5$ BMG were performed in parallelized environments, such as our local 128 core cluster, or Teragrid Ranger resources [64]. First, we ran short versions of the same H-RMC simulations, varying the model size and number of processors to study how our program scales in a massively parallel environment. Figure 13(a) shows H-RMC speed (MC steps/second) vs. number of cores used for parallelization on Ranger. It showed that the Monte Carlo step time is nearly independent of system size, because the

simulation speed of big model is only ~7% slower than that of small model, despite having ~3 time as many atoms. This means that the hutch-algorithm and MPI in our H-RMC is efficient. Figure 13(a) also demonstrates that we can achieve significantly faster calculations with increasing numbers of cores. The code speedup with number of cores is shown compared to perfect linear scaling in Figure 13(b). The results showed that the efficiency decreases as a function of numbers of cores, and the code is achieving 40% efficiency with 208 cores compared to 16 cores. The test was performed with up to only 208 cores because the maximum number of cores for parallelization in our current code is set by the number of beam orientations in the FEM calculation. We do not expect 100% speedup efficiency by using more cores because only the $I(k)$ calculation in the code was parallelized, and some I's unavoidably take longer to calculate than others when the atom movements occur beyond the periodic boundary condition.

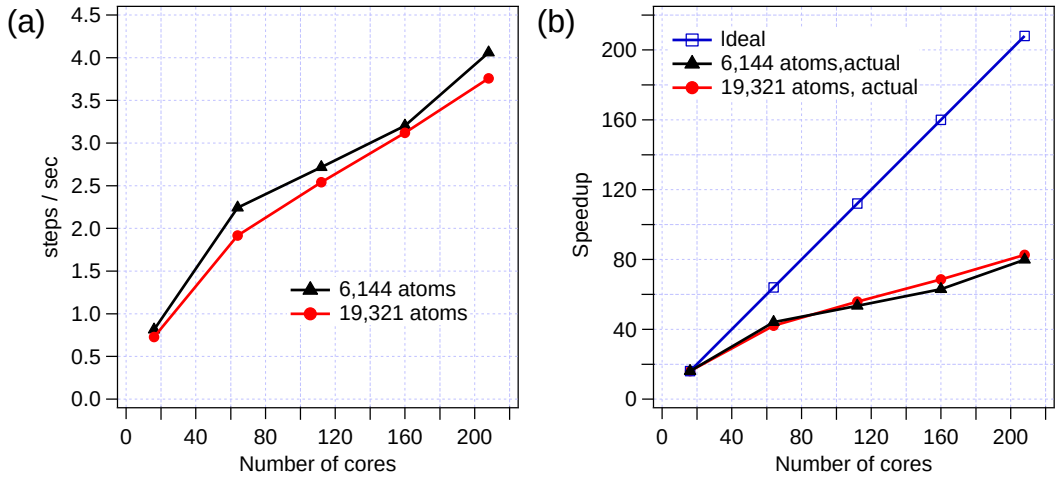

Figure 13. (a) H-RMC steps/second vs. number of cores on Ranger with two models with different sizes; (b) H-RMC speedup vs. number of cores on Ranger with two models with different sizes, compared to a perfect linear scaling.

In the H-RMC simulations, the total cost function, Eq. 8, was minimized with step-wise quenching scheme. The models of $Zr_{50}Cu_{45}Al_5$ were used for starting configurations with a density determined from the low-*r* portion of the XRD *G*(*r*) [86]. The models with 1,425 atoms in a $(2.83)^3 nm^3$ cubic box were generated by LJ-DRP, relaxed with EAM potential, and used as starting configurations. The models were then fit separately against the *V*(*k*)'s from 4 different thermal conditions – as-quenched, annealed at 300°C for 10 minutes, annealed at 300°C for 60 minutes, annealed 435°C for 2 minutes. The EAM was used for all conditions, but no *G*(*r*) was used in these simulations. The *s* in Eq. 9 was determined by combining an estimated Stobbs factor of 3 [92] and a scaling factor between the model thickness and the experimental sample thickness, following $V \sim 1/t$ relationship in Stratton et al. [51]. The γ for *V*(*k*) was determined empirically to make the EAM energy and the χ^2-*V*(*k*) relax in a similar trend through the quench, so it varied for different experimental data. Typically, a number between 1 and 3 was selected for γ.

From the H-RMC output models, we counted the Voronoi polyhedra (VP) of SRO surroundings of each atom using a code provided by Drs. Hao and Kramer. First employed by Finney [33], the Voronoi indices identify the type of polyhedron drawn around each atom using the same construction as the 1st Brillouin zone. The polyhedron types are typically presented in indices <*n3, n4, n5, n6*>, where *n* is the number of *x*-edged faces in the polyhedron. For example, a perfect icosahedron would have an indices <0, 0, 12, 0>, and a FCC cluster would have indices <0, 6, 0, 8>. The polyhedra with high *n5* values are generally considered to be quasi-icosahedral clusters. In VP counting, we selected a nearest neighbor cutoff of 0.35nm which is the high-end limit of the 1st peak in the experimental *G*(*r*). Faces that are too small, less than 1% of the total surface area of the polyhedron, were ignored in the counting, and this is similar to what Sheng et

al. did [31, 93]. In the VP counting results, VP types that occurred less than 1% of the total number of atoms were considered to be statistically insignificant and ignored.

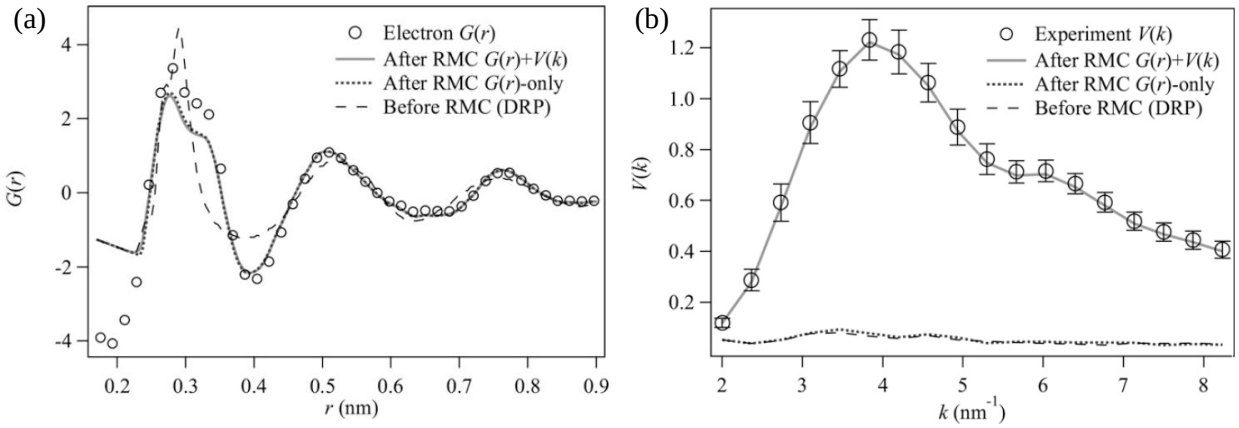

Figure 14. (a) $G(r)$ simulated before RMC and after RMC on $G(r)+V(k)$ and $G(r)$-only, compared to experimental $G(r)$. (b) $V(k)$ simulated before RMC and after RMC on $G(r)+V(k)$ and $G(r)$-only, compared to experimental $V(k)$ [65].

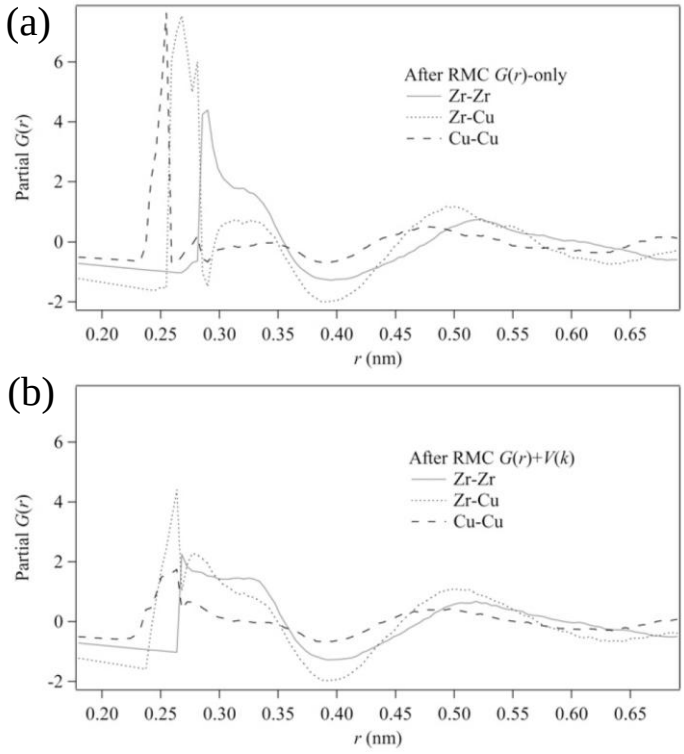

Figure 15. Partial $G(r)$s of Zr–Zr, Zr–Cu, and Cu–Cu pairs from (a) after RMC $G(r)$-only, and (b) RMC $G(r)+V(k)$ [65].

4. 3. RMC results

4. 3. 1. RMC of $Zr_{54}Cu_{38}Al_8$ BMG

Figure 14(a) shows the simulated $G(r)$ after a χ^2 convergence compared to the $G(r)$'s before the simulation and the experimental $G(r)$ [65]. The converged $G(r)$ from RMC $G(r)$-only simulation is also shown for comparison. The fit to the experimental $G(r)$ is good in both RMC $G(r)$+$V(k)$ and RMC $G(r)$-only, except for the 1st peak area where there is mismatch in the peak amplitude. This mismatch could not be removed by changing the density of the model, so we believe this is due to the artifact in the experimental $G(r)$ created by the numerical Fourier transform from the reduced density function, $\varphi(k)$ [76]. The Fourier transform tends to create artifacts at low r in $G(r)$ if the k range in $\varphi(k)$ is insufficient [76]. The k in our experiment was limited by the instrument to ~35.4nm^{-1}, which is much smaller than the k range of more typically used $\varphi(k)$ from synchrotron XRD (~100nm^{-1}). RMC could not fit the high 1st peak because the flaw in the data was mostly in the low r region, and fitting the 1st peak would have increased the 2nd and 3rd peaks and therefore increased the χ^2. The $G(r)$'s from RMC $G(r)$+$V(k)$ and RMC $G(r)$-only look identical, but their constituents, the partial $G(r)$'s, are significantly different, and the RMC $G(r)$+$V(k)$ have more realistic partial $G(r)$'s, as shown in Figure 15 [65]. The RMC $G(r)$-only model generated unrealistic partial $G(r)$'s reflecting the hard sphere cutoffs, but the RMC $G(r)$+$V(k)$ made more realistic partials that overlap each other. The $V(k)$ must have additionally confined the g_2 because it has a weak g_2 dependence as well as the stronger g_3 and g_4 dependence.

Figure 14(b) shows the simulated $V(k)$ before and after the RMC simulation, and the $V(k)$ from RMC $G(r)$-only [65]. The $V(k)$ from the model before RMC and the $V(k)$ from RMC $G(r)$-only do not show any peaks. This shows that the DRP does not have any MRO structure, and

that using only the $G(r)$ in RMC does not generate MRO structure that matches the experiment. $V(k)$ for the RMC $G(r)+V(k)$ model is an essentially perfect fit to the experimental $V(k)$, so the refinement has generated MRO in the model without changing the total $G(r)$. $V(k)$ adds new information about the nanometer scale structure to the refinement and improves the uniqueness of the resulting model. The perfect agreement with $V(k)$ indicates that the model is still not completely unique, but the space of possible models has been significantly restricted.

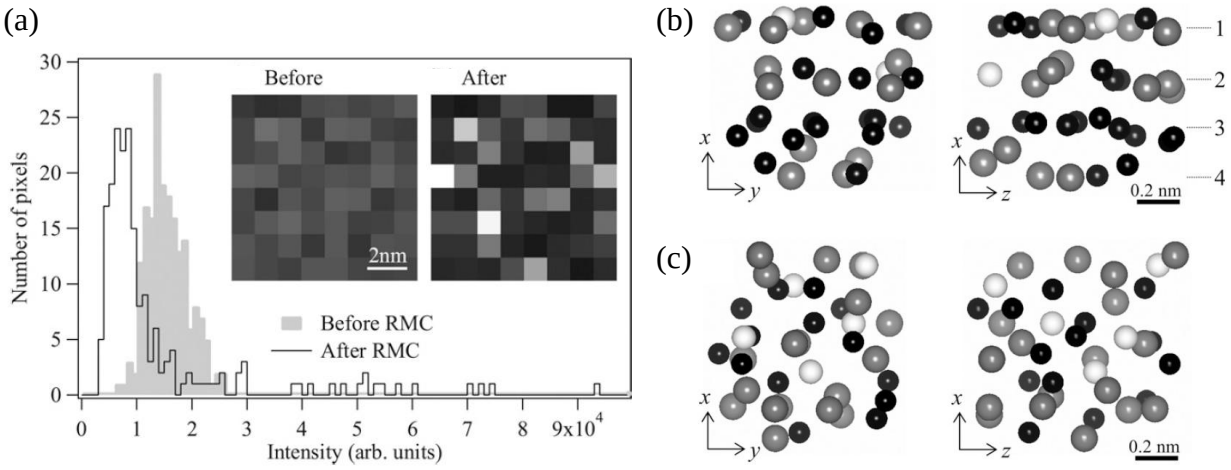

Figure 16. (a) Histogram of pixel intensities before and after RMC. Insets show simulated images of the model before, and after RMC, on the same greyscale. Atom arrangements in (b) the bright pixel column and (c) the dark pixel column along and perpendicular to the beam direction. Only part of the columns are shown. The gray, black, white atoms are Zr, Cu, and Al, respectively [65].

The histograms of $I(k)$ taken from all 192 pixels from the models before and after RMC show that the I's from some pixels increased while the others decreased after RMC, increasing the $V(k)$ (Figure 16(a)) [65]. Example simulated DF images before and after RMC are presented in the inset. The simulated intensity of each pixel which depends on the atomic structure in a column projected in that pixel, so the intensity difference between the pixels is due to the local difference in atomic structure. The atoms in the bright pixel column, Figure 16(b), have plane-like MRO ~1nm in length, while the atoms in the dark pixel column shown in Figure 16(c) appear thoroughly disordered. The MRO in Figure 16(b) is aligned to the beam direction, which is caused by the flat Ewald sphere approximation which sets all Bragg angles to zero [65]. The MRO is confined in a column, but it extends across the periodic boundary conditions of the model, making it effectively infinite in one direction. This columnar MRO is not realistic because the MRO in real BMG must be isotropic and close to a 3D cluster. A full kinematic diffraction calculation of $I(\mathbf{r}, k, Q)$ will give more accurate plane orientations, but it will also be more computationally expensive. The MRO roughly correspond to the pixel size, so they extend over ~1nm laterally. The interplanar spacing of the MRO in Figure 16(b) is about 0.26nm, which is the inverse of the 1st peak position at k = 3.8nm^{-1}, so the pseudo-planar structures like those in Figure 16(b) are the structural origin of the $V(k)$ signal of the model. The MRO in this simulation, however, does not seem to contain any chemical order.

These first RMC refinements against $V(k)$ provided two important insights. First, FEM must be sensitive to the plane-like MRO in the BMG structure. The detailed internal structure of the MRO, however, is not yet available in this simulation due to the lack of chemical order and the anisotropy of the MRO. Second, the addition of FEM data in RMC also constrained the partial $G(r)$'s, so it more stringently confined the structure at both short and medium range.

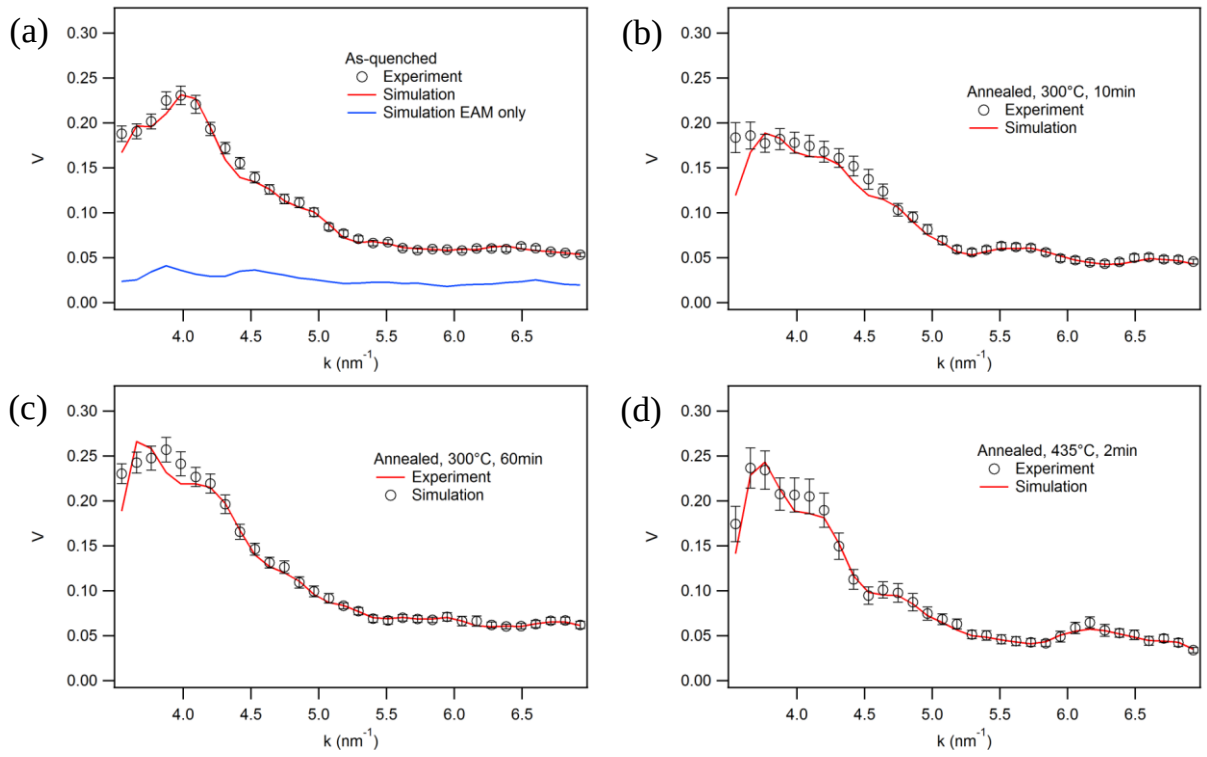

Figure 17. Simulated $V(k)$'s from the models relaxed against the EAM potential and experimental $V(k)$'s of $Zr_{50}Cu_{45}Al_5$ BMG with different thermal history: (a) as-quenched, (b) annealed at 300°C for 10 minutes, (c) annealed at 300°C for 60 minutes, and (d) annealed at 435°C for 2 minutes. The simulated $V(k)$ from a model relaxed only with EAM MC is presented in (a) for comparison. The $V(k)$ data with R=2nm was used [64].

4. 3. 2. H-RMC of $Zr_{50}Cu_{45}Al_5$ BMG

Figure 17 shows the simulated $V(k)$'s from the models relaxed against the experimental $V(k)$'s of the $Zr_{50}Cu_{45}Al_5$ samples with different thermal history and EAM potential [64]. R was 2nm in all 4 cases. The agreement between the simulation and the experiment is good for all 4 cases, but not always perfect, as seen in the k~3.5nm^{-1} region in Figure 17(b). $V(k)$ simulated for the model relaxed only with EAM MC is also presented in Figure 17(a) for comparison. It does not show any peak in $V(k)$, suggesting that using the EAM potential alone cannot generate a realistic structure at the nanometer scale, similar to what DRP model showed in Figure 14(b)

[65]. Figure 18 shows the total and partial $G(r)$'s from all 4 H-RMC models compared to the $G(r)$'s from the EAM-MC model. In Figure 18(a), the experimental total $G(r)$ from as-quenched material is also presented for comparison. Partial $G(r)$'s for only Zr-Zr, Zr-Cu, and Cu-Cu bondings are shown, because the partial $G(r)$'s containing Al atoms are noisy due to the small number of Al atoms. In all 4 H-RMC models, the total and partial $G(r)$'s are basically the same as the $G(r)$'s from the EAM-only model, suggesting that the SRO structure of the model was mostly confined by the EAM potential, and the change in $V(k)$ did not influence $G(r)$. The agreement between the simulated total $G(r)$ and experimental $G(r)$ is not perfect because the H-RMC did not fit against the experimental $G(r)$. In particular, the systematic shift of all the peaks to smaller r suggests that the EAM potential has shorter equilibrium distances than the experiment. However, the amplitudes of the peaks are in good agreement with experiment.

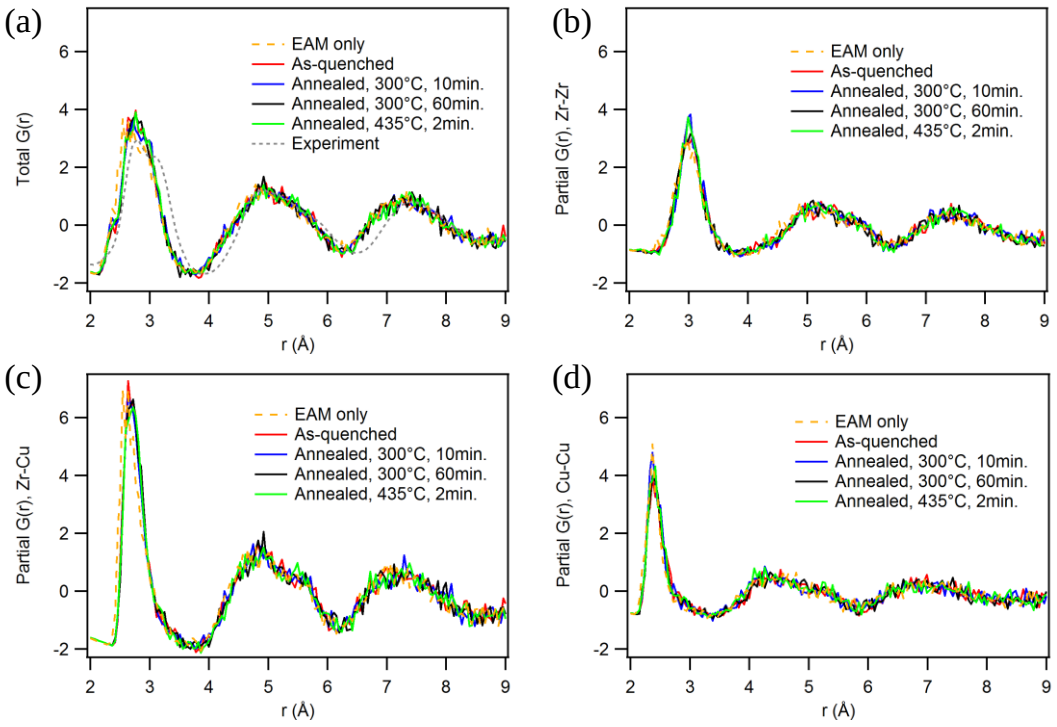

Figure 18. The total and partial XRD $G(r)$'s from all four H-RMC models compared to the $G(r)$'s from the EAM-MC model. In (a), the experimental $G(r)$ from as-quenched material was also presented. Partial $G(r)$'s for only Zr-Zr, Zr-Cu, and Cu-Cu bondings are shown.

Voronoi Indices	Percent of 5fold in a cluster	Notes
0 0 12 0		
0 0 12 0	100%	Perfect Icosahedron
(0 0 12 2	85.7%)	
0 1 10 x		Quasi-icosahedral clusters
0 1 10 2	76.9%	
0 1 10 4	66.7%	
0 2 8 x		
0 2 8 0	80.0%	
0 2 8 4	57.1%	
0 3 6 x		Mixed clusters
0 3 6 0	66.7%	
(0 3 7 2	58.3%)	
0 3 6 5	42.9%	
(1 2 5 4	41.7%)	
0 4 4 x		Crystal-like clusters (Non-icosahedra)
0 4 4 2	40.0%	
0 4 4 6	28.6%	
0 5 2 x		
0 5 2 5	16.7%	
0 5 2 6	15.4%	

Table 2. Voronoi indices of SRO clusters found in the model in the order of the percent of pentagons among all types of faces in a cluster.

We counted the VP population for the models from all 4 cases in Figure 17. In all the models, we observed a large population of icosahedral and quasi-icosahedral clusters, such as <0, 0, 12, 0> and <0, 2, 8, 2>, consistent with what Cheng et al. reported in their MD simulation with the same potential [22]. More importantly, we noticed that the population of VP varies model by model. To quantify the change in population of VP, we first divided the VP types into 5 categories by the number of pentagons in the polyhedral - <0, 0, 12, 0>, <0, 1, 10, x>, <0, 2, 8,

x>, <0, 3, 6, x>, and <0, 4, 4, x> + <0, 5, 2, x>, where x is typically a number between 0 and 4. Table 2 summarizes the VP types found in the model in the order of the number of pentagons in a cluster. By the percent of pentagons in a cluster, we considered the 5 types as perfect icosahedral, quasi-icosahedral, mixed, and crystal-like clusters, respectively, as depicted in Table 2. The <0, 4, 4, x> and <0, 5, 2, x> were regarded as non-icosahedra in Cheng et al. [22], but we consider these types as crystal-like clusters because of their high number of square and hexagonal faces, and similarity to the perfect FCC and HCP clusters, <0, 6, 0, 8> and <0, 6, 0, 2>, respectively. A small number of other cluster types, such as <0, 3, 7, 2>, was included in a category that has similar indices and similar percent of pentagons.

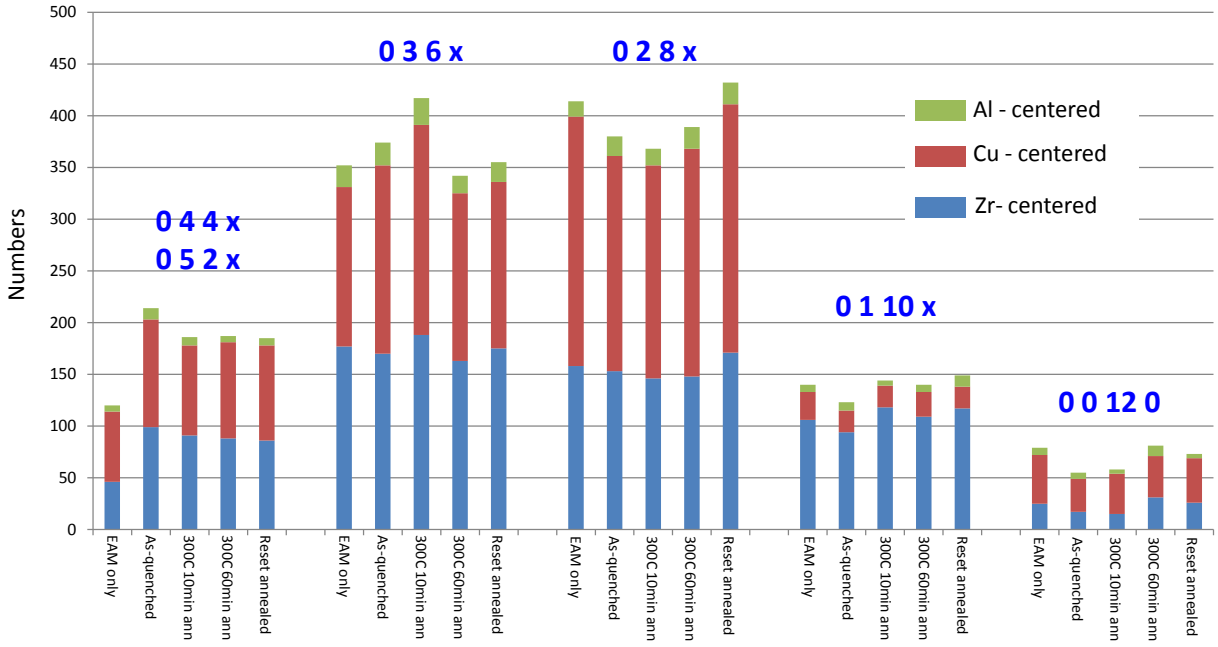

Figure 19. A histogram of VP types for different H-RMC models. The VP data for EAM-only MC model was also shown for comparison.

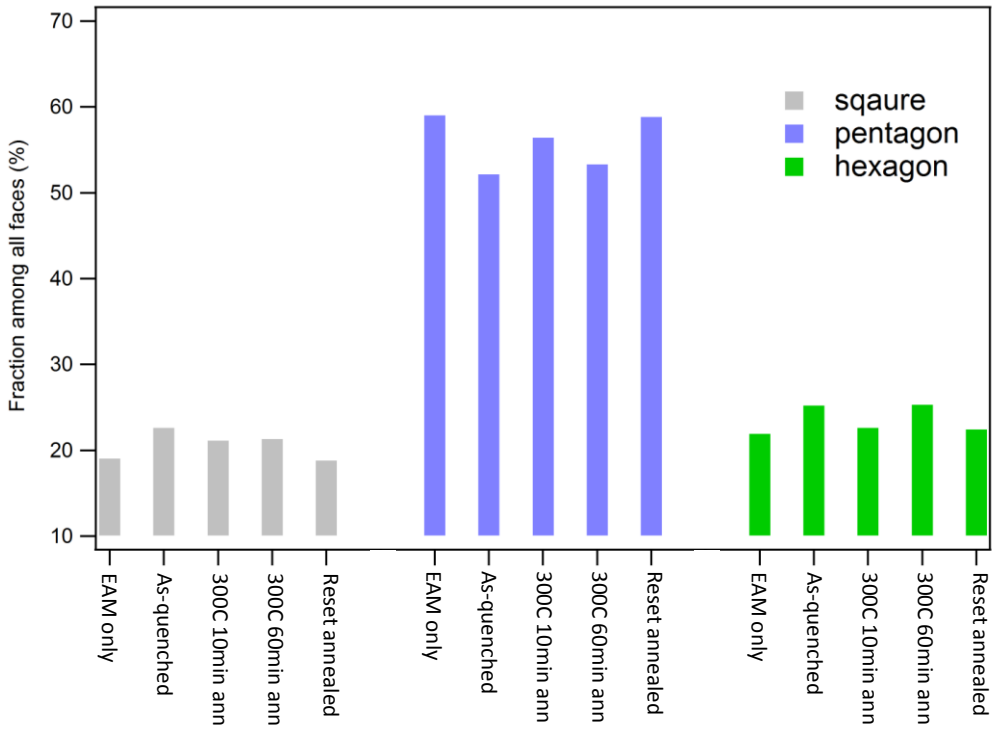

Figure 20. Fractions of squares, pentagons, and hexagons among all faces of polyhedra in 5 different models.

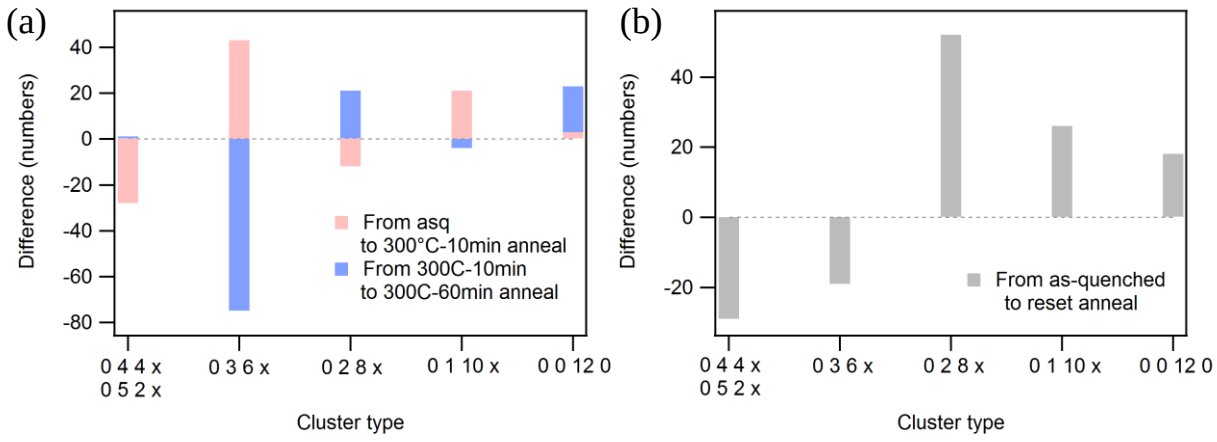

Figure 21. The change in VP numbers between the annealing conditions, calculated from the histogram in Figure 19.

The histogram of VP's is shown in Figure 19. In general, the EAM-only model showed the highest population of perfect icosahedra and icosahedral-like clusters. There were fewer such clusters in the as-quenched and the 300°C, 10 minute annealed model. However, the populations of icosahedral clusters are again high in the 300°C, 60 minute annealed and the reset annealed models. The mixed icosahedra, <0, 3, 6, x>, showed a somewhat opposite trend to the icosahedral clusters. For the crystal-like clusters, the numbers are small in the EAM-only model, while the as-quenched model had the maximum population of these types of clusters. The annealed models showed similar population of the crystal-like clusters. The histogram also showed that the <0, 1, 10, x> clusters mostly had Zr atoms at their centers, while <0, 0, 12, 0>, and <0, 2, 8, x> preferred Cu atoms at their centers. The mixed icosahedra and the crystal-like clusters did not show any particular preference for their centers, as the proportion of their center atom types approximately matched the global composition. Figure 20 shows the fractions of squares, pentagons, and hexagons among all faces of polyhedra in 5 different models. The fraction of pentagons shows a pattern similar to the patterns of icosahedral clusters in Figure 19, while the squares and the hexagons approximately follow the patterns of the crystal-like and the mixed clusters. One apparent exception is the increase in the fraction of pentagon in 300°C, 10 minute annealed model, and this is a relative consequence of the decrease of hexagons in this model.

From the VP histogram, we calculated the change in VP numbers between the annealing conditions, as shown in Figure 21. In Figure 21(a), the crystal-like clusters decreased and the <0, 3, 6, x> clusters increased between the as-quenched model and the 300°C, 10 minute annealed model. Between the 300°C, 10 minute annealed model and the 300°C, 60 minute annealed model, the <0, 3, 6, x> decreased, but the <0, 2, 8, x> and the <0, 0, 12, 0> increased. This

suggests that the crystal-like clusters may change into more icosahedral-like clusters as time progresses in a sub-T_g annealing. The number of the <0, 1, 10, x> clusters, however, increased by the 10 minute annealing, so this type of cluster may stabilize earlier than the other icosahedral clusters. Such stabilization of icosahedral clusters is also seen in the reset annealing data in Figure 21(b), but both the crystal-like clusters and the <0, 3, 6, x> decreased, while the others increased. This suggests that in the reset anneal, where the thermal energy is high, the stabilization of icosahedral clusters may happen much faster than in a sub-T_g annealing.

As seen in Figure 19, the population of icosahedral clusters in the 300°C, 60 minute annealed model and the reset annealed model almost matched the population of those in the EAM-only model, but there was one significant difference: the EAM-only model did not generate any peak in $V(k)$, as shown in Figure 17(a). All four H-RMC models have more crystal-like clusters, so the crystal-like clusters, if they are nanometer sized, might be responsible for the peaks in $V(k)$. However, the $V(k)$ peak shapes are all different in 4 different conditions, as seen in Figure 17. The as-quenched model had maximum at k~4.0nm^{-1}, while the annealed models had their maxima near k~3.7nm^{-1}. Our hypothesis is that both the crystal-like clusters and the icosahedral clusters are responsible for the peaks in $V(k)$, but each correspond to different peaks, which overlap in the experimental $V(k)$. One cluster, regardless of the type, is about 0.7nm in diameter and may be too small to make a peak in $V(k)$, which is primarily sensitive to the MRO scale. For example, the EAM-only model has a high density of icosahedral clusters, but it generates no signal in $V(k)$, as shown in Figure 17(a). Therefore we think what makes peaks in $V(k)$ may be a nanometer scale pseudo planar structure, similar to the MRO in our previous RMC (Figure 16(b)), made by some alignment of the SRO clusters. An alignment of crystal-like

cluster is intuitively easy, but knowing whether the alignment of icosahedral cluster is really responsible for the peaks in $V(k)$ requires a direct investigation of the atom positions in the model.

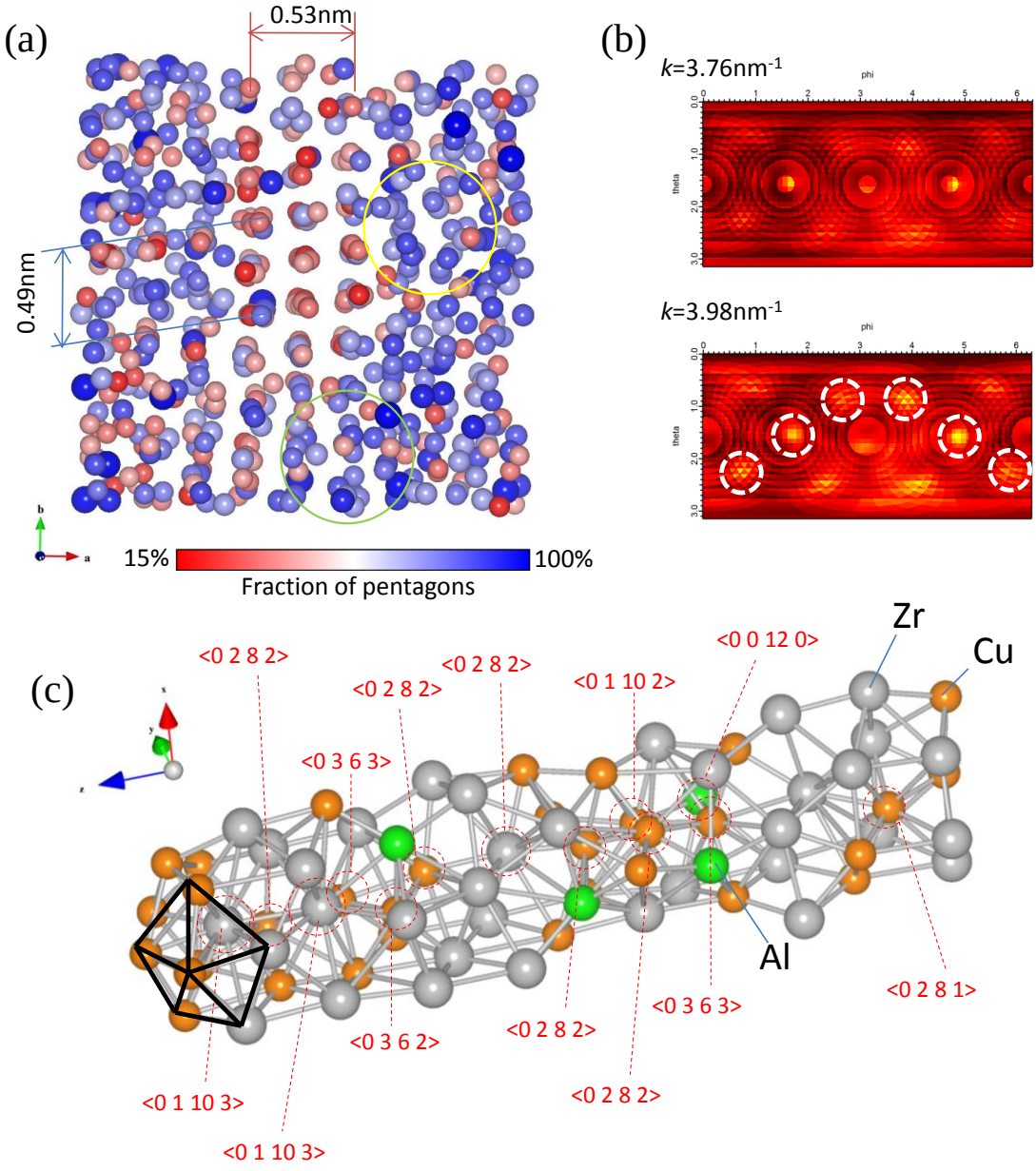

Figure 22. (a) The MRO region of the 300°C, 60 minute annealed model. The atoms are colored by the degree of 5 fold in their surroundings. (b) Surface maps of 3D Fourier transform of the entire 300°C, 60 minute annealed model, at k=3.76 and 3.98 nm^{-1}. The white dashed circles in the k= 3.98nm^{-1} map indicate the six fold rotational symmetries. (c) MRO extracted from the yellow circled region of the model in (a), and identification of VP inside the MRO. Atoms are colored by atomic species in (c) [64].

The H-RMC generated plane-like MRO in the model, and the MRO from 300°C, 60 minute annealed model was shown in Figure 22(a). The atoms are colored by the fraction of pentagons in their VP, not by their atom types. The atoms with blue atoms have icosahedral VP around them, while the red ones are the centers of crystal-like clusters. The MRO is similar to the plane-like MRO in our previous RMC (Figure 16(b)), but the planes are oriented in many different directions, and the MRO in the center has a nearly 6 fold rotational symmetry, which is a signature of a crystal-like order. In the nearly 6 fold region, the atom colors are more reddish, meaning that the cluster types of the center area are more likely to be crystal-like ones. Such gatherings of crystal-like clusters were not found in the EAM-only model. Adjacent to the center 6 fold area, there are some gatherings of blue atoms, especially in the area indicated by the yellow and the green circles in the figure. Those regions have plane-like order in this orientation of the model, but only with nearly 2-fold symmetry in this orientation, so they are plane-like MRO formed by gathering of icosahedral clusters. Figure 22(b) shows the surface maps of 3D Fourier transform of the entire 300°C, 60 minute annealed model, at k=3.76 and 3.98nm^{-1}. The yellow hot spots on the map are potential diffraction maxima, analogous to reciprocal lattice points from a crystal, so the hot spots represent the order in the model that diffracts to that particular vector k. The map for k=3.76nm^{-1} shows two hot spots, meaning the order has 2 fold rotational symmetry. k=3.76nm^{-1} corresponds to an interplanar spacing of ~0.27nm, so the map matches the vertically aligned plane-like order in Figure 22(a). k=3.98nm^{-1}, however, shows many hot spots, and we identified them as two different 6 fold symmetries crossing each other one of which is shown by the white dashed circles in the figure. k=3.98nm^{-1} corresponds to an interplanar spacing of ~0.25nm, so it matches the horizontally aligned order, and the diagonally aligned order in Figure 22(a). The vertically aligned order in k=3.76nm^{-1} map also appears in the

k=3.98nm^{-1} map, so the planar order is not strict, and diffracts the electron beam in a broad range of k.

The types of rotational symmetry must be introduced by refinement against the combination of $V(k)$ and the EAM potential. Intuitively, having an MRO that diffracts into multiple directions must be easier for H-RMC to increase the $V(k)$, but the order at k=3.76nm^{-1} generated only 2 fold symmetry. This implies that the order at k=3.76nm^{-1} would be energetically unstable if it was formed in 6 fold symmetry, unlike the order at k=3.98nm^{-1}. H-RMC essentially generated two different MRO in the region shown in Figure 22(a), but the two MROs are not entirely separated: the vertical 2 fold order formed as an extension of one of the orientations of the 6 fold order. We do not know, at this point, whether this is something physical. If it is an unphysical artifact, the H-RMC must have generated this combined MRO due to the small size of the model, and two types of ordered cluster might be separated in a larger model.

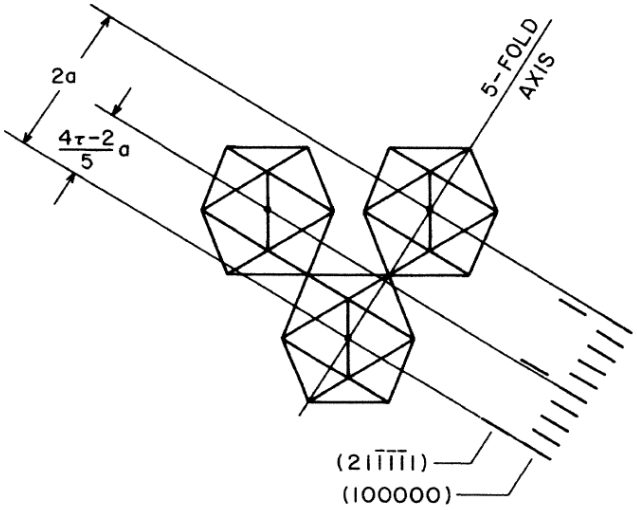

Figure 23. Three vertex-connected icosahedra, illustrating the projected displacements along a 5 fold axis [97].

As shown in the color scales of the atoms in Figure 22(a), the 2 fold order is compatible with the icosahedral clusters, while the 6 fold order is compatible to the crystal-like clusters. We extracted the order in the yellow circled region of the model in Figure 22(a), and identified the types VP clusters, and displayed in Figure 22(c). The MRO consists of chains of icosahedral clusters, with various types of center atoms. The MRO might have formed longer in one direction because of the limitations of the simulation discussed in section 4. 3. 1, but the MRO in Figure 22(c) still provides important insights about the structure: some icosahedral clusters may be aligned in a real BMG, generating the necessary MRO-size correlated cluster to give rise to the peak in $V(k)$ at k=3.76nm^{-1}. The MRO of aligned icosahedra in our H-RMC model is similar to the other possible MROs seen previously [22, 30, 31], but different in a sense that this MRO has a particular interplanar spacing that matches a peak in $V(k)$. This icosahedral MRO may be related to the icosahedral quasi-crystals seen in BMG [94] or boron carbide systems [95, 96], but we particularly found similarity between our icosahedral MRO and the possible stacking mechanism of icosahedra suggested by Stephens and Goldman [97] and Torquato et al. [98]. Stephens and Goldman [97] suggested that a particular arrangement of icosahedra, shown in Figure 23, can produce Bragg peaks, which is consistent to with our H-RMC model.

The final energy per atom in the EAM MC was -4.82eV, while the H-RMC relaxed models had slightly higher final energy per atom, between -4.803 and -4.80eV. However, the MRO ordered regions do not have a higher energy than the rest of the model, so the increase of the energy might be due to the interface between the MRO and non-MRO region.

4. 3. 3. New structural model for BMGs and its implications

From FEM and H-RMC simulations, we discovered several important new features of the nanometer scale structure of BMGs and its evolution. First, we found crystal-like MRO in BMG for the first time. The crystal-like MRO degraded by the reset annealing at $1.06T_g$, so it is not same as the quenched in nuclei seen in Al-based marginal glasses [59]. In Al-based glasses, the MRO evolved to FCC nanocrystals by annealing, but such crystallization was not observed in Zr-based BMG systems. Kelton et al. reported a significant order in the BMG liquids detected by XRD [99]. If the order in the liquid is related to the crystal-like order, the BMG might inherit the order from liquids through glass transition. Second, our H-RMC generated crystal-like clusters and icosahedral MRO in nanometer scale which other MD simulations of BMG [22, 31, 32] failed to capture. As discussed in section 1. 1, the MD simulations may not generate realistic MRO due to their fast quench rate. The structure from MD simulations may be a maximally icosahedral and maximally disordered state which real glasses never reach. The finding of the crystal-like and the icosahedral MRO in H-RMC is supported by the angular correlation analysis of FEM nanodiffraction patterns, which is discussed in Chapter 5. Finally, our H-RMC simulations suggested that the structural relaxation of BMG involves a transformation of crystalline-like MRO into icosahedral-like MRO. The exothermic heat that DSC detected may be due to a free volume annihilation at the interface of crystalline-like MRO and the icosahedra-rich region.

We confirmed that the icosahedral-like clusters can gather, align, and diffract electron beam at certain *k*. Questions remain regarding what drives the alignment of these clusters. The alignment does not seem to have happened by chance because it did not occur in the EAM-only MC model where the icosahedra density is the highest. One possibility we can suggest is that the

alignment of icosahedra may be likely to happen near the crystalline-like MRO as an extension of the plane-like order, as shown in Figure 22. When the crystal-like MRO changes into a icosahedral MRO by structural relaxation, it is likely that some planar order from the crystal-like MRO still remains, but with a slight change in the interplanar spacing. This may be related to the peak shift in $V(k)$ by annealing.

The MRO found in H-RMC may be directly connected to the GFA of BMG. As discussed in section 1. 1, MD simulations disagree on the glass forming mechanism in close packed systems, such as BMGs. While stabilization of icosahedral clusters in glass transition are typically seen in MD simulations [22, 29, 31, 32], Tanaka et al. suggested that crystal-like MRO in a glass system may stabilize earlier and act as a center of atomic mobility slowdown [35]. The structure from H-RMC in Figure 22(a) may imply a combination of those two mechanisms. The crystal-like MRO formed earlier in glass transition, or inherited from the liquid, may promote the formation of icosahedral clusters nearby, and help freezing the structure. These results also connect with the idea that crystal nucleation is suppressed in good glass formers by structural frustration, or competition of several different phases. Our model suggests a competition between a crystal-like and quasi-icosahedral structures, or, taken to the ordered extreme, a competition between crystalline and quasi-crystalline order [94].

The MRO we found in H-RMC models may be connected to STZs which are the key to understanding the plastic flow of BMGs. An STZ deforms by shearing on a slip plane inside itself, so the crystalline-like MRO we found seems like a better candidate for an STZ because it has many possible slip planes, just like a crystal structure does, compared a group of icosahedral clusters with much lower symmetry. If there is indeed any relationship between the crystalline-like MRO and the STZ, the degradation of those MRO by annealing may affect the mechanical

properties of the BMG. Experimental measurement of the mechanical properties under these same annealing conditions is currently underway by our collaborators, Melgarejo and Dr. Stone.

Chapter 5. Angular Correlations

The nanodiffraction patterns, as shown in Figure 9, show Bragg diffraction speckles from local MRO, so the rotational symmetry of the speckles as a function of scattering vector magnitude, *k*, should reveal the rotational symmetry of the internal structure of the MRO. However, identifying the important symmetry in nanodiffraction is a difficult task, because the TEM sample may contain several ordered regions through the thickness whose speckles may overlap, and the important speckles may be hidden amongst scattering from statistically insignificant structures. To study this subtle rotational symmetry in the FEM nanodiffraction, we adopted the angular correlation function, $C_k(\Delta)$, from Wochner et al. [100, 101].

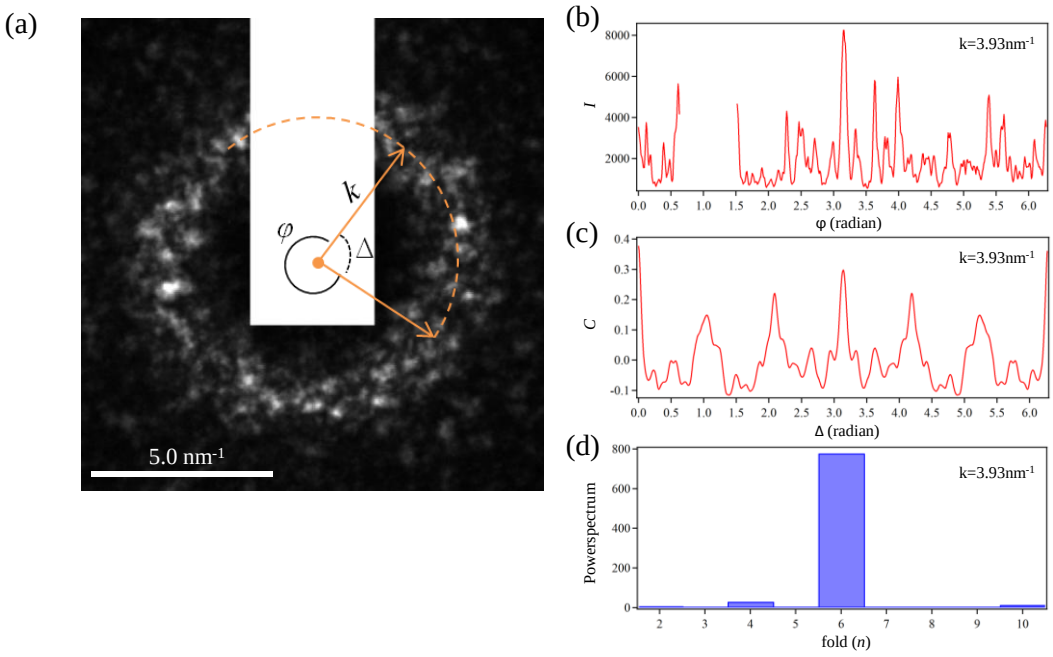

Figure 24. (a) Example of a nanodiffraction acquired with 2nm diameter probe. (b) $I(\varphi)$, (c) $C(\Delta)$, and (d) P_n at k=3.93nm^{-1}of the pattern in (a). The white block in (a) masks the beam stop.

$$C_k(\Delta) = \frac{\langle I(k,\varphi) I(k,\varphi+\Delta) \rangle_\varphi - \langle I(k,\varphi) \rangle_\varphi^2}{\langle I(k,\varphi) \rangle_\varphi^2}, \quad \text{(Eq. 13)}$$

where $I(k, \varphi)$ is the diffracted intensity in polar coordinates. $C_k(\Delta)$ shows the correlations between two intensities at the same k, separated by angle Δ, averaged over the entire angle φ, as indicated in the Figure 24(a). Wochner et al. used $C_k(\Delta)$ analysis on coherent synchrotron diffraction patterns from dispersed PMMA colloid samples, and discovered that the colloids occasionally form order that has 4 or 5 fold symmetry [100]. Gibson et al. recently applied the $C_k(\Delta)$ analysis to electron nanodiffraction, and measured a crystalline topology from the 2 fold symmetry in amorphous Si samples [102].

To apply $C_k(\Delta)$ to our FEM nanodiffraction, we first converted the 2D nanodiffraction into a 1D polar coordinate graph, as shown in an example in Figure 24. Figure 24(b) shows the unwrapped $I(k, \varphi)$ at k=3.93nm^{-1} from the diffraction pattern in Figure 24(a). Figure 24(c) is the corresponding $C(\Delta)$ calculated from the $I(k, \varphi)$ in Figure 24(b). While there is no identifiable symmetry in $I(k, \varphi)$, $C(\Delta)$ shows 6 distinctive peaks with same intervals, which means a strong 6 fold symmetry. We further calculated the power spectrum, P_n, from the $C_k(\Delta)$ to quantitatively extract the symmetry in $C_k(\Delta)$. The P_n of $C_k(\Delta)$, shown in Figure 24(d), has even greater sensitivity to the rotational symmetry. In this case, it has a single strong peak at n = 6.

We calculated the average of $P_n(k)$ over 2,077 nanodiffraction patterns from as-quenched $Zr_{50}Cu_{45}Al_5$ BMG ribbons. Figure 25(a) shows the average $P_n(k)$ for n=2 to 10. Near the 1st diffraction ring (k~4.0nm^{-1}), n=2 (Figure 25(b)) is higher than any other n, so Friedel symmetry is the dominant feature. n=4 and 6, which are signatures of crystalline order, are also relatively strong at similar k, but have several peaks in k, especially n=6. This suggests that there may be different types of crystalline-like MRO with different interatomic spacings, which is consistent

to our findings discussed in Chapter 3 and 4. The shape of $P_n(k)$ is different for n=2, 4, and 6, so the n=4 and 6 data are not purely the result of random combinations of n=2. We also observe a peak for n=10 in Figure 25(b). n=10 fold is a 5-fold symmetry doubled by Friedel conjugates, so it may arise from icosahedral-like MRO.

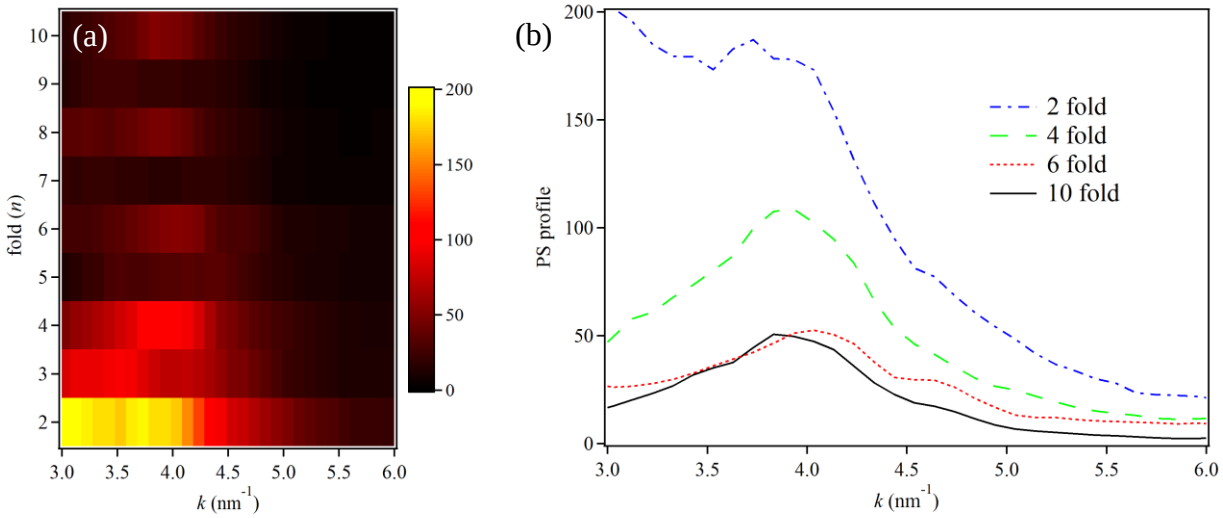

Figure 25. (a) Average $P_n(k)$, and (b) line profiles at n = 2, 4, 6, and 10.

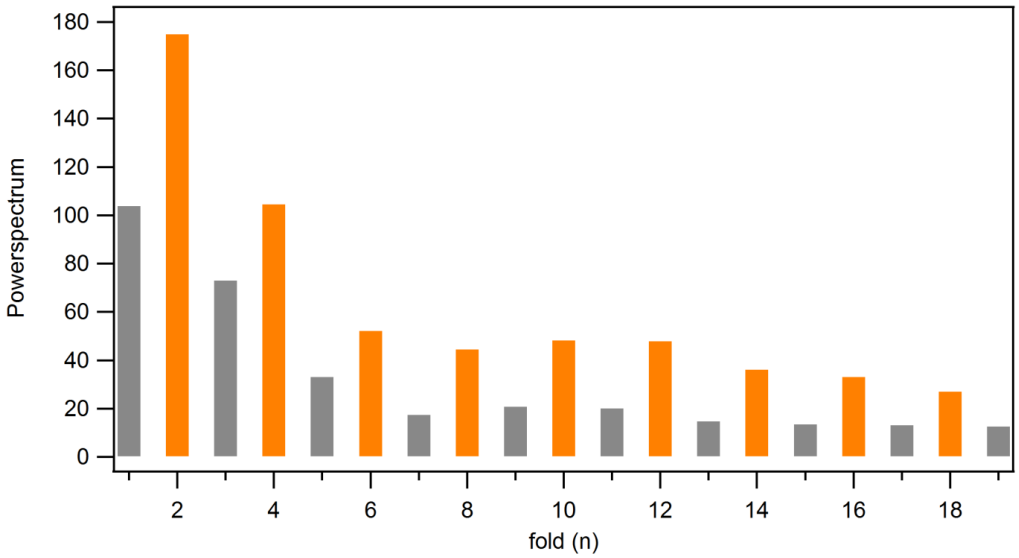

Figure 26. Power spectrum vs. rotational symmetry order at k=3.93nm^{-1}.

Figure 26 shows the power spectrum vs. n from same data at k=3.93nm^{-1}. It shows that even numbered n's are consistently higher than the odd numbered ones. A power spectrum from randomly arranged single speckles is monotonically decreasing, so Figure 26 does have some excess correlation for even n's. The $P_n(k)$ may contain some artifacts: the higher order symmetries, such as n=4, 6, and 10, may be in part the result of random arrangement of 2 fold pairs [103], but we do not know the amount of the artifact contribution at this time. We also confirmed that the effect of beam stop to the power spectrum is small and ignorable.

In summary, angular correlation analysis of FEM nanodiffraction patterns revealed the signatures of both the crystal-like and the icosahedral MRO, which is consistent with our findings in FEM experiments and H-RMC simulation, although fully statistically rigorous analysis requires additional work.

Chapter 6. Conclusion

We developed a state-of-art FEM procedure in a C_s-corrected STEM that excels any previous FEM works in several ways. First, the coherence of electron probe was increased, so the V signal from the sample was maximized. Second, the VRFEM was measured at constant coherence up to 11nm scale which is almost 3 times larger than the previous FEM experiments. Third, energy filtered nanodiffraction was applied to FEM, so the quality of the nanodiffraction data has greatly increased. Finally, we identified and corrected the contribution from sample thickness variations using Z-contrast images as references.

We also developed a H-RMC simulation combining FEM $V(k)$ and an EAM interatomic potential. Compared to MD modeling using only interatomic potentials or the RMC modeling using only conventional diffraction data, our H-RMC modeling substantially reduces the space of models generated by refinement, especially in nanometer scale. We experimentally detected the signs of icosahedral clusters by angular correlation analysis of FEM nanodiffraction patterns. We believe this is by far the most direct experimental confirmation of icosahedral-like order in any glass structure.

Our findings suggest that Zr-based BMG contains two different kinds of MRO in its nanoscale structure: an MRO that resembles crystalline structure, and an MRO that consists of aligned icosahedral SRO clusters. The MRO may be directly related to BMG's important properties, such as glass forming ability and plastic deformation. We detected a clear change in atomic structure by structural relaxation for the first time, and found that the structural relaxation involves a transition of crystalline-like MRO to icosahedral MRO.

Chapter 7. References

[1] W.L. Johnson, Bulk Glass-Forming Metallic Alloys: Science and Technology, *MRS Bulletin*, **24**, 10, 42-56 (1999).

[2] A. Inoue, Stabilization of metallic supercooled liquid and bulk amorphous alloys, *Acta Materialia*, **48**, 279-306 (2000).

[3] A. L. Greer, Metallic glasses on the threshold, *Materials Today* **12,** 1-2, 14-22 (2009).

[4] C. C. Hays, C. P. Kim, and W. L. Johnson, Microstructure controlled shear band pattern formation and enhanced plasticity of bulk metallic glasses containing in situ formed ductile phase dendrite dispersions, *Phys. Rev. Lett*. **84**, 2901-2904 (2000).

[5] R. Vaidyanathan, M. Dao, G. Ravichandran, and S. Suresh, Study of mechanical deformation in bulk metallic glass through instrumented indentation, *Acta Materialia* **49**, 3781-3789 (2001).

[6] Z. Bian, G. He, and G. L. Chen, Microstructure and mechanical properties of as-cast Zr52.5Cu17.9Ni14.6Al10Ti5 bulky glass alloy, *Scripta Materialia* **43**, 1003-1008 (2000).

[7] M. L. Morrison, R. A. Buchanan, A. Peker, W. H. Peter, J. A. Horton, and P. K. Liaw, Cyclicanodic-polarization studies of a Zr41.2Ti13.8Ni10Cu12.5Be22.5 bulk metallic glass, *Intermetallics* **12**, 1177-1181 (2004).

[8] A. Kawashima, H. Habazaki, and K. Hashimoto, Highly corrosion-resistant Ni-based bulk amorphous alloys, *Materials Science and Engineering A* **304**, 753-757 (2001).

[9] Z. P. Lu, C. T. Liu, J. R. Thompson, and W. D. Porter, Structural amorphous steels, *Phys. Rev. Lett*. **92**, 245503 (2004).

[10] S. J. Poon, G. J. Shiflet, F. Q. Guo, and V. Ponnambalam, Glass formability of ferrous- and aluminum-based structural metallic alloys, *J. Non-Cryst. Sol*. **317**, 1-9 (2003).

[11] B. J. Park, H. J. Chang, D. H. Kim, W. T. Kim, K. Chattopadhyay, T. A. Abinandanan, and S. Bhattacharyya, Phase separating bulk metallic glass: a heirarchical composite, *Phys. Rev. Lett*. **96**, 245503 (2006).

[12] Y. C. Kim, J. H. Na, J. M. Park, D. H. Kim, J. K. Lee, and W. T. Kim, Role of nanometer-scale quasicrystals in improving the mechanical behavior of Ti-based bulk metallic glasses, *Appl. Phys. Lett*. **83**, 3093-3095 (2003).

[13] T. Wada, A. Inoue, and A. L. Greer, Enhancement of room-temperature plasticity in a bulk metallic glass by finely dispersed porosity, *Appl. Phys. Lett*. **86**, 251907 (2005).

[14] J. Schroers, C. Veazey, and W. L. Johnson, Amorphous metallic foam, *Applied Physics Letters* **82**, 370-372 (2003).

[15] A. H. Brothers and D. C. Dunand, Porous and foamed amorphous metals, *Mat. Res. Bull*. **32**, 639-643 (2007).

[16] B. Zhang, D. Q. Zhao, M. X. Pan, W. H. Wang, and A. L. Greer, Amorphous metallic plastic, *Phys. Rev. Lett*. **94**, 205502 (2005).

[17] J. Schroers and N. Paton, Amorphous metal alloys form like plastics, *Advanced Materials & Processes* **164**, 61-63 (2006).

[18] A. H. Brothers, R. Scheunemann, J. D. DeFouw and D. C. Dunand, Processing and structure of open-celled amorphous metal foams, *Scripta Materialia* **52**, 4, 335-339 (2005)

[19] G. Kumar, H. X. Tang, and Jan Schroers, Nanomoulding with amorphous metals, *Nature* **457**, 12, 868 (2009).

[20] A. Inoue, T. Zhang and T. Masumoto, Matererials Transactions, *Japan Institute of Metals* **31**, 3, 177-183, (1990).

[21] D. Wang, H. Tan, and Y. Li: Multiple maxima of GFA in three adjacent eutectics in Zr–Cu–Al alloy system – A metallographic way to pinpoint the best glass forming alloys. *Acta Mater.* **53**, 2969-2979 (2005).

[22] Y. Q. Cheng, E. Ma, and H. W. Sheng, Atomic level structure in multicomponent bulk metallic glass, *Phys. Rev. Lett*. **102**, 245501 (2009).

[23] H. E. Fischer, A. C. Barnes, and P. S. Salmon, Neutron and x-ray diffraction studies of liquids and glasses, *Rep. Prog. Phys*. **69**, 233-299 (2006).

[24] P. M. Voyles and John. R. Abelson, Medium-range order in amorphous silicon measured by fluctuation electron microscopy, *Solar Energy Materials & Solar Cells* **78**, 85-113 (2003).

[25] Y. Waseda: *Anomalous X-Ray Scattering for Materials Characterization* (Springer, 2002).

[26] J. J. Rehr and R. C. Albers, Theoretical approaches to x-ray absorption fine structure, *Reviews of Modern Physics* **72**, 3, 621 (2000).

[27] L V Heimendahl, Metallic glasses as relaxed Bernal structures, *J. Phys. F: Met. Phys.* **5** L141 (1975).

[28] T. Egami and Y. Waseda, Atomic size effect on the formability of metallic glasses, *J. Non-Cryst. Sol*. **64**, 113-134 (1984).

[29] J. H. Honeycutt and H. C. Anderson, Molecular Dynamics Study of Melting and Freezing of Small Lennard- Jones Clusters, *J. Phys. Chem* **91**, 4950-4963 (1987).

[30] D. B. Miracle, A structural model for metallic glasses, *Nature Materials* **3**, 697-702 (2004).

[31] H.W. Sheng, W.K. Luo, F.M. Alamgir, J.M. Mai, and E. Ma, Atomic packing and short-to-medium-range order in metallic glasses, *Nature* **439**, 419 (2006).

[32] M. I. Mendelev, D. J. Sordelet, and M. J. Kramer, Using atomistic computer simulations to analyze x-ray diffraction data from metallic glasses, *Journal of Applied Physics* **102**, 043501 (2007).

[33] J. L. Finney, Random Packings and the Structure of Simple Liquids. I. The Geometry of Random Close Packing, *Proc. R. Soc*. A **319**, 479 (1970)

[34] D. Ma, A. D. Stoica, and X. -L. Wang, Power-law scaling and fractal nature of medium range order in metallic glasses, *Nature Materials* **8**, 30-34 (2009).

[35] Hajime Tanaka, Takeshi Kawasaki, Hiroshi Shintani and Keiji Watanabe, Critical-like behaviour of glass-forming liquids, *Nat. Mater*. **9** 324-331 (2010).

[36] U. R. Pedersen, T. B. Schrøder, J. C. Dyre, and P. Harrowell, Geometry of Slow Structural Fluctuations in a Supercooled Binary Alloy, *Phys. Rev. Lett.* **104**, 105701. (2010).

[37] G. Adam and J. H. Gibbs, On the temperature dependence of cooperative relaxation properties in glass-forming liquids, *J. Chem. Phys*. **43**, 1, 139 (1965).

[38] A. Slipenyuk and J. Eckert, Correlation between enthalpy change and free volume reduction during structural relaxation of Zr55Cu30Al10Ni5 metallic glass, *Script. Mater.* **50**, 39-44 (2004).

[39] W. Dmowski, C. Fan, M.L. Morrison, P.K. Liaw, T. Egami, Structural changes in bulk metallic glass after annealing below the glass-transition temperature, *Materials Science and Engineering A*, **471**, 125–129 (2007).

[40] F. Spaepen, A microscopic mechanism for steady state inhomogeneous flow in metallic glass, *Acta Metall*. **25**, 407-415 (1977).

[41] A. S. Argon, Plastic deformation in metallic glasses, *Acta Metal.* **27**, 47-58 (1979).

[42] Y. Shi and M. L. Falk, Strain localization and percolation of stable structure in amorphous solids, *Phys. Rev. Lett*. **95** 095502 (2005).

[43] J. Li, F. Spaepen, and T. C. Hufnagel, Nanometre-scale defects in shear bands in a metallic glass, *Phil. Mag. A* **82**, 2623-2630 (2002).

[44] P. S. Steif, F. Spaepen, and J. W. Hutchinson, Strain localization in amorphous metals, *Acta Metall.* **30**, 447-455 (1982).

[45] J. J. Lewandowski and A. L. Greer, Temperature rise at shear bands in metallic glasses, *Nature Materials* **5**, 15-18 (2006).

[46] Y. E. Kalay and M. J. Kramer, unpublished data.

[47] M. M. J. Treacy, J. M. Gibson, L. Fan, D. J. Paterson, and I. McNulty, Fluctuation microscopy: a probe of medium range order, *Rep. Prog. Phys.* **68**, 2899-2944 (2005).

[48] J. M. Gibson, M. M. J. Treacy, and P. M. Voyles, Atom pair persistence in disordered materials from fluctuation microscopy, *Ultramicroscopy* **83**, 169-178 (2000).

[49] P. M. Voyles and D. A. Muller, Fluctuation microscopy in the STEM, *Ultramicroscopy* **93**, 147-159 (2002).

[50] Jinwoo Hwang and P. M. Voyles, Variable Resolution Fluctuation Electron Microscopy on Cu-Zr Metallic Glass Using a Wide Range of Coherent STEM Probe Size, *Microscopy and Microanalysis* **17,** 67-74 (2011).

[51] W. G. Stratton, and P. M. Voyles, A phenomenological model of fluctuation electron microscopy for a nanocrystal/amorphous composite, *Ultramicroscopy* **108**, 727-736 (2008).

[52] S. N. Bogle, L. N. Nittala, R. D. Tweston, P. M. Voyles, and J. R. Ableson, Size Analysis of Nanoscale Order in Amorphous Materials by Variable-Resolution Fluctuation Electron Microscopy, *Ultramicroscopy* **110,** 10, 1273–1278 (2010).

[53] S.N. Bogle, P.M. Voyles, S.V. Khare, and J.R. Abelson: Quantifying nanoscale order in amorphous materials, simulating fluctuation electron microscopy of amorphous silicon, *J. Phys. Cond. Mat.* **19**, 455204 (2007).

[54] P.M. Voyles, J.E. Gerbi, M.M.J. Treacy, J.M. Gibson, and J.R. Abelson, Absence of an abrupt phase change from polycrystalline to amorphous in silicon with deposition temperature, *Physical Review Letters* **86**, 5514-5517 (2001).

[55] P. M. Voyles, N. Zotov, S. M. Nakhmanson, D. A. Drabold, J. M. Gibson, M. M. J. Treacy, and P. Keblinski, Structure and physical properties of paracrystalline atomistic models of amorphous silicon, *J. Appl. Phys.* **90**, 9 (2001).

[56] M. M. J. Treacy, J. M. Gibson, and P. J. Keblinski, Paracrystallites found in evatporated amorphous tetrahedral semiconductors, *J. of Non-Cryst. Sol*. **231**, 99-110 (1998).

[57] X. Chen, J. P. Sullivan, T. A. Friedmann, and J. M. Gibson, Fluctuation microscopy studies of medium-range ordering in amorphous diamond-like carbon films, *Appl. Phys. Lett*. **84**, 15, 2823 (2004).

[58] B. S. Lee, G. W. Burr, R. M. Shelby, S. Raoux, C. T. Rettner, S. N. Bogle, K. Darmawikarta, S. G. Bishop and J. R. Abelson, Observation of the Role of Subcritical Nuclei in Crystallization of a Glassy Solid, *Science* **326**, 980-984 (2009).

[59] W. G. Stratton, J. Hamann, J. H. Perepezko, X. Mao, S. V. Khare, and P. M. Voyles, Aluminum nanoscale order in amorphous Al92Sm8 measured by fluctuation electron microscopy, *Appl. Phys. Lett*. **86**, 141910 (2005).

[60] T. C. Hufnagel, Cang Fan, R. T. Ott, J.Li, and S. Brennan, Controlling shear band behavior in metallic glasses through microstructural design, *Intermetallics* **10**, 1163-1166 (2002).

[61] S.O. Hruszkewycz, T. Fujita, M.W. Chen, and T.C. Hufnagel, Selected area nanodiffraction fluctuation electron microscopy for studying structural order in amorphous solids, *Scripta Mat.* **58**, 303-306 (2008).

[62] T.L. Daulton, K.S. Bondi, and K.F. Kelton, Nanobeam diffraction fluctuation electron microscopy technique for structural characterization of disordered materials - Application to $Al_{88-x}Y_7Fe_5Ti_x$ metallic glasses, *Ultramicroscopy* **110**, 1279-1289 (2010).

[63] Jinwoo Hwang, Hongbo Cao, and P. M. Voyles, Nanometer-scale structural relaxation in Zr-based bulk metallic glass, *Mater. Res. Soc. Symp. Proc.* **1048**-Z05-04 (2008).

[64] Jinwoo Hwang, Z. H. Melgarejo, Y. E. Kalay, M. J. Kramer, D. A. Stone and P. M. Voyles, Nanoscale relaxation mechanism in Zr-based metallic glass investigated by fluctuation

microscopy (in preparation).

[65] Jinwoo Hwang, A. M. Clausen, Hongbo Cao and P. M. Voyles, Reverse Monte Carlo structural model for a zirconium-based metallic glass incorporating fluctuation microscopy medium-range order data, *J. Mater. Res.* **24**, 10, 3121-3129 (2009).

[66] P. M. Voyles, *Fluctuation Electron Microscopy of Medium-Range Order in Amorphous Silicon* (Dissertation, 2001).

[67] F. Yi, P. Tiemeijer, and P. M. Voyles, Flexible formation of coherent probes on an aberration-corrected STEM with three condensers, *Journal of electron microscopy* (to be published)

[68] F. Yi and P. M. Voyles, *Ultramicroscopy* (to be published)

[69] L. Fan, D. Paterson, I. McNulty, M. M. J. Treacy, and J. M. Gibson: Fluctuation X-ray microscopy, a novel approach for the structural study of disordered materials, *Journal of Microscopy* **225**, 1, 41–48 (2007).

[70] R.K. Dash, P.M. Voyles, J.M. Gibson, M.M.J. Treacy, and P. Keblinski, A quantitative measure of medium-range order in amorphous materials from transmission electron micrographs, *J. Phys. Condens. Matter* **15**, S2425 (2003).

[71] L. A. Freeman, A. Howie, A. B. Mistry, and P. H. Gaskell, *The Structure of Non-Cryst. Mats.* edited by P. H. Gaskell (p.245, Taylor and Francis, London, 1976).

[72] D. T. Schweiss, Jinwoo Hwang, and P. M. Voyles, Inelastic and elastic mean free path of FIB made bulk metallc glass samples, *Microscopy and Microanalysis* (to be submitted)

[73] P. M. Voyles, J. E. Gerbi, M. M. J. Treacy, J. M. Gibson, and J. R. Abelson, Absence of an abrupt phase change from polycrystalline to amorphous in silicon with deposition temperature. *Physical Review Letters* **86**, 5514-5517 (2001).

[74] Hao Chen and Jian-Min Zuo, Structure and phase separation of Ag–Cu alloy thin films, *Acta Mater*. **55**, 1617-1628 (2007).

[75] E.J. Kirkland, *Advanced Computing in Electron Microscopy* (Plenum, NY, 1998).

[76] D. J. H. Cockayne and D. R. Mckenzie, Electron diffraction analysis of polycrystalline and amorphous thin films, *Acta Cryst*. *A* **44**, 870-878 (1988).

[77] Z. H. Melgarejo and D. A. Stone, to be published.

[78] P. M. Voyles, N. Zotov, S. M. Nakhmanson, D. A. Drabold, J. M. Gibson, M. M. J. Treacy, and P. Keblinski, Structure and physical properties of paracrystalline atomistic models of amorphous silicon, *J. Appl. Phys.* **90**, 9 (2001).

[79] D. A. Keen and R. L. Mcgreevy, Structural modelling of glasses using reverse Monte Carlo simulation, *Nature* **344**, 423-425 (1990).

[80] R. L. McGreevy, Reverse Monte Carlo modeling, *J. Phys.: Condens. Matter* **13**, R877-R913 (2001).

[81] Parthapratim Biswas, Raymond Atta-Fynn, and D. A. Drabold, Reverse Monte Carlo modeling of amorphous silicon, *Phys. Rev. B* **69**, 195207 (2004).

[82] G. Opletal, T. C. Petersen, D. G. McCulloch1, I. K. Snook, and I. Yarovsky, The structure of disordered carbon solids studied using a hybrid reverse Monte Carlo algorithm, *J. Phys. Condens. Matter* **17**, 2605 (2005).

[83] P. Biswas, D. N. Tafen, R. Atta-Fynn and D. A. Drabold, The inclusion of experimental information in first principles modelling of of materials, *J. Phys.: Cond. Matter* **16**, S5173-S5182 (2004).

[84] P. Biswas and D. A. Drabold, Inverse approach to atomistic modeling: Apllications to a-Si:H and g-$GeSe_2$, *J. of Non-cryst. Sol*. **354**, 2697-2701 (2008).

[85] P. Biswas, R. Atta-Fynn, S. Charkraborty and D. A. Drabold, Real space information from fluctuation electron microscopy, applications to amorphous silicon. *J. Phys.: Cond. Matter* **19**, 455202 (2007).

[86] M. J. Kramer and Y. E. Kalay, unpublished data

[87] J. Puthoff and D.S. Stone, Unpublished data.

[88] Allen, L.J., et al., Lattice-resolution contrast from a focused coherent electron probe: part I, *Ultramicroscopy*, **96**, 47-63 (2003).

[89] W. G. Stratton and P. M. Voyles, Comparison of fluctuation electron microscopy theories and experimental methods, *J. Phys.: Condens. Matter* **19**, 455203 (2007).

[90] Jinwoo Hwang and P. M. Voyles, Hybrid reverse Monte Carlo simulation incorporating fluctuation microscopy (in preparation)

[91] M. P. Allen and D. J. Tildesley, *Computer simulation of liquids*, (Carendon Press, Oxford, 1987).

[92] M.J. H.gtch and W.M. Stobbs, Quantitative comparison of high resolution TEM images with image simulations, *Ultramicroscopy* **53**, 191 (1994).

[93] Private communication, E. Ma, 2009.

[94] B. S. Murty and K. Hono, Nanoquasicrystallization of Zr-based metallic glasses, *Materials Science and Engineering* A **312**, 253-261 (2001).

[95] R. Lazzari, N. Vast, J. M. Besson, S. Baroni, and A. Dal Corso, Atomic structure and vibrational properties of icosahedral B_4C Boron Carbide, *Phys. Rev. Lett*. **83**, 16, 3230 (1999).

[96] Bingqing Wei, Robert Vajtai, Yung Joon Jung, Florian Banhart, Ganapathiraman Ramanath, and Pulickel M. Ajayan, Massive icosahedral boron carbide crystals, *J. of Phys. Chem. B* **106**, 23, 5807 (2002).

[97] P. W. Stephens and A. I. Goldman, Sharp diffraction maxima from an icosahedral glass, *Phys. Rev. Lett*. **56**, 11, 1168 (1986).

[98] S. Torquato and Y. Jiao, Dense packings of the Platonic and Archimedean solids, *Nature* **460**, 13, 876 (2009).

[99] V. Wessels, A. K. Gangopadhyay, K. K. Sahu, R. W. Hyers, S. M. Canepari, J. R. Rogers, M. J. Kramer, A. I. Goldman, D. Robinson, J. W. Lee, J. R. Morris, and K. F. Kelton: Rapid chemical and topological ordering in supercooled liquid $Cu_{46}Zr_{54}$, *Phys. Rev.* B **83**, 094116 (2011).

[100] P. Wochner, C. Gutt, T. Autenrieth, T. Demmer, V. Bugaev, A. D. Ortiz, A. Duri, F. Zontone, G. Grübel, and H. Dosch, X-ray cross correlation analysis uncovers hidden local symmetries in disordered matter, *PNAS* **106**, 28, 11511(2009).

[101] M. Altarelli, R. P. Kurta, and I. A. Vartanyants, X-ray cross-correlation analysis and local symmetries of disordered systems: General theory, *Phys. Rev.* B **82** (2010) 104207.

[102] J. M. Gibson, M. M. J. Treacy, T. Sun, and N. J. Zaluzec, Substantial Crystalline Topology in Amorphous Silicon, *Phys. Rev. Lett*. **105** 125504 (2010).

[103] Private communication, T. Sun, 2010.